# Mn(III) porphyrins as potential MRI contrast agents for diagnosis and MRI-guided therapy

Geraldes, Carlos F.G.C.; Castro, M. Margarida C.A.; Peters, Joop A.

**DOI**
10.1016/j.ccr.2021.214069

**Publication date**
2021

**Document Version**
Accepted author manuscript

**Published in**
Coordination Chemistry Reviews

# Mn(III) porphyrins as potential MRI contrast agents for diagnosis and MRI-guided therapy

Carlos F.G.C. Geraldes[a,b,*], M. Margarida C. A. Castro[a], Joop A. Peters[c*]

[a] *Department of Life Sciences and Coimbra Chemistry Centre, Faculty of Science and Technology, University of Coimbra, Calçada Martim de Freitas, 3000-456 Coimbra, Portugal*

[b] *CIBIT/ICNAS, University of Coimbra, Azinhaga de Santa Comba, 3000-548 Coimbra, Portugal*

[c] *Department of Biotechnology, Delft University of Technology, Van der Maasweg 9, 2629 HZ Delft, The Netherlands*

[*] Corresponding authors: geraldes@uc.pt (C.F.G.C. Geraldes), j.a.peters@tudelft.nl (J.A.Peters)

Dedicated to José J. G. Moura and Isabel Moura at the occasion of their 70th birthday

**Abstract**

Mn(III) porphyrins have great potential as Gd-free MRI contrast agents because both the cation and the ligand have interesting properties. The redox properties of the Mn(III)-ion can be exploited for the preparation of reactive oxygen species for therapy. Moreover, the porphyrin ligand allows these complexes to have a high affinity for tumor tissues. The inherent properties of the porphyrin ligands make these systems attractive for photothermal, photodynamic, and sonodynamic therapies. Therefore, these systems are attractive for the development of theranostics for MRI-guided therapy. For the magnetic field strengths at which most clinical MRI machines operate at present (0.5 - 1.5 T), the longitudinal relativity of low-molecular-weight complexes is even higher than that of the classical Gd-based contrast agents. This review gives an overview of the developments in the field of Mn(III) porphyrin contrast agents during the last 30 years.

**Contents**




**Key words**

Relaxivity; theranostics; photothermal therapy; photodynamic therapy; chemotherapy

*Abbreviations*: BBB, blood brain barrier; BSA, bovine serum albumin; CD, cyclodextrin; CT, chemotherapy; DCE, dynamic contrast enhanced; DFT, density functional theory; DOTA, 1,4,7,10-tetraazacyclododecane-1,4,7,10-tetraacetate; DSPE, 1,2-Distearoyl-sn-glycero-3-phosphorylethanolamine; DOX, doxorubicin; DTPA, diethylenetriamine-N,N,N′,N′′,N′′-pentaacetate; GSH, glutathione; HSA, human serum albumin; i.p. intraperitoneal; i.v., intravenous; MOF, metal–organic framework; MRI, magnetic resonance imaging; mPEG, polyethylene glycol monomethyl ether; NCT, neutron capturing therapy; NIR, near infrared; NMOF, nanoscale metal–organic framework; NMRD, nuclear magnetic resonance dispersion; NP, nanoparticle; PA, photo-acoustic; PDT, photodynamic therapy; PEG, polyethylene glycol; PLA, polylactic acid; PK, pharmacokinetics; PS, photosensitizer; PTT, photothermal therapy; RBC, red blood cell; RNS, reactive nitrogen species; ROS, reactive oxygen species; RT, radiotherapy; SBM, Solomon-Bloembergen-Morgan; SDT, sonodynamic therapy; SNO, *S*-nitrosothiol; SOD, superoxide dismutase; SW, shock wave; US, ultra sound; zfs, zero-field splitting.

**1. Introduction**

The intensity of a signal of a voxel in an MRI scan mainly depends on the local amount of water protons and their NMR relaxation rates. Therefore, the contrast can be modulated by enhancing the relaxation rates through paramagnetic agents. Since the introduction of MRI into clinics in the 1980s, Gd(III) polyamino carboxylate complexes including GdDTPA and GdDOTA have been used for this purpose [1–5]. Over the last decade, concerns have arisen due to some incidences of nephrogenic systemic fibrosis and observations of accumulation of Gd(III) in patients after multiple MRI exams [6–9]. This has stimulated the interest in Gd-free contrast agents (CAs) [10]. Mn-based CAs are attractive alternatives because both the high-spin $d^5$ cation Mn(II) ($S$ = 5/2) and the $d^4$ cation Mn(III) ($S$ = 2) are strong paramagnets whereas free Mn-cations are considerably less toxic than free Gd(III) since they play a role in biology such as in the anti-oxidant enzyme superoxide dismutase (SOD). However, high concentrations of Mn-ions are neurotoxic and therefore, they need to be sequestered for safe application as intravenous CA in humans. Research on Mn(II) chelates and Mn-ferrite nanoparticles (NPs) as potential MRI CAs has been reviewed recently [11–13]. In the present review, we describe the application of Mn(III) porphyrins as potential MRI CAs and theranostics. The porphyrin complexes are particularly interesting because they have been shown to localize preferentially in tumors [14,15]. This contrasts with the classical Gd-based CAs which distribute almost non-selectively over the intracellular space. Furthermore, porphyrins have interesting optical properties that make them attractive for the development of photothermal and photodynamic therapies. The multivalency of the central Mn-cation opens avenues to the development of redox responsive CAs. The focus of this review will be on relaxivity and the design of theranostics. The synthesis of Mn(III) porphyrin systems will not be discussed since that topic has been discussed in a previous review [16].

**2. Structure and some properties of Mn(III) porphyrins**

Mn(III) is not stable in aqueous solutions, stabilization requires coordination with a multidentate ligand such as a porphyrin and a phthalocyanine. Particularly, Mn(III) porphyrin systems have been extensively studied. In these complexes, Mn(III) is octahedrally coordinated through strong bonds with the equatorial $N_4$-porphyrin ligand and relatively weakly with two remaining axial ligands. Calculations with the *ab initio* and density functional theory (DFT) have shown that the Mn(III) ion (effective ionic radius = 0.785 Å) fits perfectly in the porphin cavity in a coplanar fashion within the porphin plane and forms a complex with an Mn(III)-bound $H_2O$ molecule at each of the axial positions on either side of the plane ($q$ = 2), whereas the larger Mn(II) ion (effective ionic radius = 0.970 Å) exhibits significant out-of-porphin plane displacement and binds to a single $H_2O$ molecule [17]. It should be noted that porphyrin complexes with the even larger Gd(III) ion (effective ionic radius = 1.193 Å) are less stable. This is, for example, demonstrated by a rapid decrease of the relaxivity of Gd(III)$TPPS_4$ (for structures, see Figs 1 and 2) due to dissociation of Gd(III), whereas Mn(III)$TPPS_4$ is stable in human plasma for at least 9 days [18]. The axial water ligands in Mn(III) porphyrins may bridge to form dimers or oligomers [19,20]. The self-association is stabilized by the $\pi$-$\pi$ interaction of the aromatic porphyrins and is destabilized by Coulomb repulsion between charged substituents and by steric strain due to bulky substituents. In the Cambridge Structural Database (CSD), 19 structures of mononuclear Mn (III) porphyrin complexes with six-coordinated Mn(III) and $q$ = 2 have recently been found. These complexes have an average distance between Mn(III) and the Mn-bound water oxygen atom (Mn-$O_{water}$) of 2.25$\pm$0.07 Å and an average Mn-$H_{water}$ distance of 2.77$\pm$0.11 Å.

Electron donating substituents at the porphyrin skeleton enhance the stability of Mn(III) porphyrins to a greater extent than the corresponding Mn(II) complexes, whereas electron-withdrawing substituents have the opposite effect. The charge density around the Mn cation is also reflected in the metal-centered reduction potential, $E_{1/2}$ for Mn(III) porphyrin/ Mn(II) porphyrin. For example, the $E_{½}$ = -194 mV and + 480 mV for Mn(III)TCP (see Figs 1 and 2 for structures) and octa-brominated Mn(II)T4MPyP, (the bromine atoms are attached to the $\beta$-pyrrole positions) respectively [21]. The Mn-cation is stabilized in the 3-valent state in Mn(III)TCP and the 2-valent state in octa-brominated Mn(II)T4MpyP. A value of $E_{½}$ between -100 to +400 mV allows Mn porphyrins to rapidly exchange electrons with diverse endogenous reactive species. Compounds with these $E_{1/2}$ may have potential as redox responsive CAs and as SOD mimics.

Two classes of Mn (III) porphyrin derivatives can be distinguished: the meso-substituted and the pyrrole-substituted (see Figs 1 and 2). The meso-substituted porphyrins are synthetic and the pyrrole-substituted porphyrins are mostly derived from natural porphyrins. Polar substituents are usually required to make them sufficiently soluble for use as CA.

In complexes with phenyl derivatives at the meso positions, the steric strain due to the interaction between the 2,6-phenyl H atoms and the pyrrole H atoms is minimized by rotation of the phenyl groups from the porphyrin plane, see for example the molecular structure of Mn(III)TPP as obtained by X-ray diffraction (Fig. 3) [22]. The more water-soluble Mn(III)$TPPS_4$ is the first and most extensively studied Mn(III) complex for application as MRI CA [14,18,23–29]. It is a $q$ = 2 complex ($E_{½}$ = -160 mV), which is stable in air and biological media, but can be easily reduced to Mn(II)$TPPS_4$ with dithionite [30]. The latter complex is not stable in air but oxidizes rapidly to the Mn(III) complex in air.

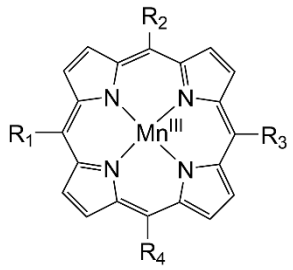


**Mn(III)TCP** $R_{1-4}$ = $COO^-$

**Mn(III)TPP** $R_{1-4}$ =

**Mn(III)TPPS$_4$** $R_{1-4}$ = $SO_3^-$

**Mn(III)TPPC$_4$** $R_{1-4}$ = $COO^-$

**Mn(III)TPP(3CM)$_4$** $R_{1-4}$ = $O-CH_2COO^-$

**Mn(III)TPPS$_3$A** $R_{1-3}$ = $SO_3^-$; $R_4$ = $NH_2$

**Mn(III)TPPS$_3$CNmPEG$_n$** $R_{1-3}$ = $SO_3^-$; $R_4$ = $C(=O)-NH-(CH_2CH_2O)_n-CH_3$

**Mn(III)TPP(mPEG$_n$)$_4$** $R_{1-4}$ = $O-(CH_2CH_2O)_n-CH_3$

**Mn(III)TPF$_4$P(mPEG$_{10-11}$)$_4$** $R_{1-4}$ = $O-(CH_2CH_2O)_{10-11}-CH_3$

**Mn(III)TPP(TMA)$_3$** $R_{1-4}$ = $-C_6H_4-N^+(CH_3)_3$

**Mn(III)T4PyP** $R_{1-4}$ = 4-pyridyl

**Mn(III)T4MPyP** $R_{1-4}$ = $-C_6H_4-N^+-CH_3$

$R_{1-4}$ = $-C_6H_4-N^+-R_5$

**Mn(III)T2MPyP** $R_5$ = $CH_3$

**Mn(III)T2EPyP** $R_5$ = $CH_2CH_3$

**Mn(III)T2BuPyP** $R_5$ = n-butyl

**Mn(III)T2HexPyP** $R_5$ = n-hexyl

**Mn(III)T2BuOEPyP** $R_5$ = $-CH_2CH_2CH_2-O-CH_3$

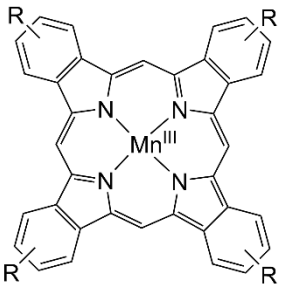


**Mn(III)PcS** R = $SO_3^-$

**Mn(III)mPEG** R = $O(CH_2CH_2O)_nOCH_3$

**Mn(III)Chol** R = $CH_2CH_2N(CH_3)_2$

**Fig. 1**. Molecular structures of Mn(III)-complexes of meso-substituted porphyrins and phthalocyanines.

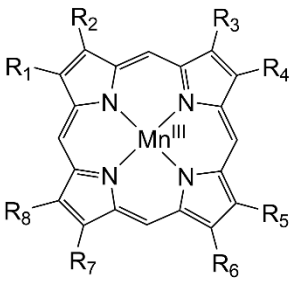

**Mn(III)PP** $R_{1,3,5,8} = CH_3$; $R_{2,4} = CHCH_2$; $R_{6,7} = CH_2CH_2COO^-$

**Mn(III)HP-IX** $R_{1,3,5,8} = CH_3$; $R_{2,4} = CH(OH)CH_3$; $R_{6,7} = CH_2CH_2COO^-$

**Mn(III)Meso** $R_{1,3,5,8} = CH_3$; $R_{2,4} = CH_2CH_3$; $R_{6,7} = CH_2CH_2COO^-$

**Mn(III)MSP** $R_{1,7} = H$; $R_{2,4,6,8} = CH_3$; $R_{3,5} = CH_2CH_3$

**Mn(III)CP1** $R_{1,3,5,7} = CH_2CH_2COO^-$; $R_{2,4,6,8} = CH_3$

**Mn(III)D24DSA** $R_{1,3,5,8} = CH_3$; $R_{2,4} = SO_3^-$ $R_{6,7} = CH_2CH_2COO^-$

**Mn(III)UROP-1** $R_{1,3,5,7} = CH_2CH_2COO^-$; $R_{2,4,6,8} = CH_2COO^-$

**Mn(III)BOPP** $R_{1,3,5,8} = CH_3$; $R_{6,7} = CH_2CH_2COO$- $R_{2,4} = CH(OH)$-$CH_2OH$ tetrakiscarborane carboxylate

**Mn(III)KADF** $R_{1,3,5,8} = CH_3$; $R_2 = CHCH_2$; $R_{6,7} = CH_2CH_2COO^-$

$R_4 =$ 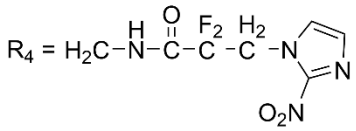

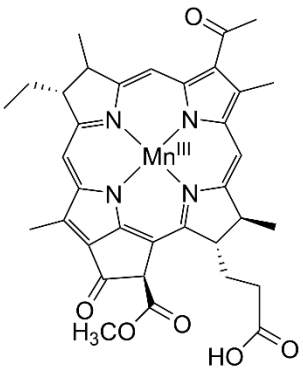

**Mn(III)BPheoid**

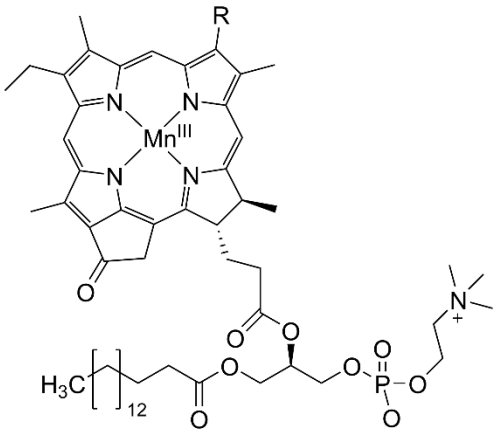

**Mn(III)HPPH-lipid 1** R = $CH{=}CH_2$

**Mn(III)HPPH-lipid 2** R= $CH(CH_3)$-O-$(CH_2)_5$-$CH_3$

**Mn(III)N-HPPH-lipid 2** R= $CH(CH_3)$-O-$(CH_2)_5$-$CH_2NH_2$

**Fig. 2.** Molecular structures of Mn(III) complexes of pyrrole-substituted porphyrins.

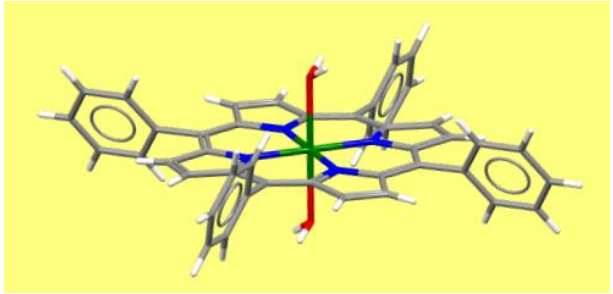

**Fig. 3.** Molecular structure of Mn(III)TPP as obtained by X-ray diffraction [22]. Retrieved from The Cambridge Crystallographic Data Centre, deposition number 116923.

## 3. Relaxivity of Mn(III) porphyrin systems

### *3.1. The inadequacy of the Solomon-Bloembergen-Morgan equations to model the relaxivities of Mn(III) porphyrins*

The efficacy of the relaxation enhancement of a potential MRI CA is usually expressed as its longitudinal or transverse relaxivity ($r_i$ with $i$ = 1,2 respectively), which is the enhancement of the longitudinal or transverse relaxation rate ($R_i = 1/T_i$) normalized for 1 mM concentration of paramagnetic ion, Mn(III) in the present case. In the vast majority of studies on Mn(III) porphyrin-based CAs, $1 \leq r_2/r_1 \leq 1.5$, which leads to an increased signal intensity (positive contrast) in $T_1$-weighted images. The relaxation enhancement of water protons by a paramagnetic complex originates from the dipole-dipole interaction between the fluctuating magnetic fields of the electron spins of the paramagnetic metal ion and the $^1$H nuclear spins of water molecules in their proximity due to three mechanisms: (*i*) the reorientation of the Mn-$H_{water}$ vector (correlation time $\tau_R$), (*ii*) the chemical-exchange of Mn(III)-bound water with the bulk (correlation time $\tau_M = k_{ex}^{-1}$), and (*iii*) the electronic relaxation (correlation time $\tau_S$).

The relaxivity can be separated into an inner-sphere contribution by water molecules exchanging between the first coordination sphere of Mn(III) and the bulk and an outer-sphere contribution due to water molecules in the bulk that diffuse in the surroundings of the metal ion without being bound to it ($r_{1,OS}$). The *in vivo* concentration of a CA needed is always very small (in the mM range) and the Mn(III)-induced chemical shifts of the water protons are negligible. Under those conditions, $r_1$ is given by Eqn (1) [31,32]. Here $T_{1M}$ is the average longitudinal relaxation time of an Mn(III)-bound water molecules and $\tau_M$ is the average residence time of water molecules in the first coordination sphere of Mn(III).

$$r_1 = \frac{q}{55556(T_{1M}+\tau_M)} + r_{1,OS} \qquad (1)$$

Koenig et al. suggested based on data of Mn(II)-DTPA that $r_{1,OS}$ of Mn(III)$TPPS_4$ is less than 5% of $r_{1,IS}$ [25] and Schaefle and Sharp have concluded from a simulation using spin and molecular dynamics calculations that this contribution was less than 2-3% [33]. To the best of our knowledge, no experimental data on aqueous solutions of $Mn^{III}$ complexes lacking inner-sphere water molecules to confirm this have been reported until now. According to the Solomon-Bloembergen-Morgan (SBM) model [2,3,5], $T_{1M}$ is governed by correlation times $\tau_{Ci}$, which are given by Eq. (2), where $\tau_{S1}$ and $\tau_{S2}$ are the longitudinal and transverse electronic relaxation times, respectively and $\tau_R$ is the rotational correlation time. Fitting of graphs of $r_1$ as a function of the magnetic field strength ($B_0$) or the $^1$H Larmor frequency (*LF*), known as nuclear magnetic resonance dispersion (NMRD) profiles, of

Gd(III) complexes with this model generally provides good estimates of the parameters governing their relaxivity.

$$\tau_{Ci}^{-1} = \tau_{Si}^{-1} + \tau_M^{-1} + \tau_R^{-1} \quad i = 1,2 \qquad (2)$$

The electronic structure of the $d^4$ ion Mn(III) is less symmetric than that of the $d^5$ ion Mn(II) and the $f^7$ ion Gd(III). Consequently, the electronic relaxation times of Mn(III) complexes are shorter ($10^{-10}$-$10^{-11}$ s) than that of Mn(II) ($10^{-8}$ s) and Gd(III) complexes ($10^{-8}$-$10^{-9}$ s) [34]. For example for Mn(III)TPPS$_4$, $T_{1M} \approx 10^{-3}$-$10^{-4}$ s, both $\tau_R$ and $\tau_s$ are in the order of magnitude of $10^{-10}$ s [33,34], whereas $\tau_M = 3.7\times10^{-8}$ [35]. Therefore, $\tau_M$ is negligible in Eqs (1) and (2) and $r_1$ is almost independent of it. Accordingly, the shapes of NMRD profiles for Mn(III) porphyrins generally differ significantly from those for Mn(II) and Gd(III) complexes. For Mn(III) porphyrins the NMRD profiles show always a maximum at 10 < LF < 40 MHz, but Gd(III) and Mn(II) complexes of low molecular weight ligands are always almost flat at LF > 10-20 MHz. Some typical examples are compiled in Fig. 4 [36–38]. These plots indicate that Mn(III) porphyrins perform optimally between 0.5 and 1.5 T (*LF* = 20-65 MHz), which is the range of $^1$H Larmor frequencies at which most clinical MRI machines operate nowadays. Moreover, the $r_1$ values of Mn(III)TPPS$_4$ are higher than those of the classical CA GdDOTA [39]. This can be explained in part by the higher $q$ value of Mn(III)TPPS$_4$: 2 as compared to 1 of GdDOTA.

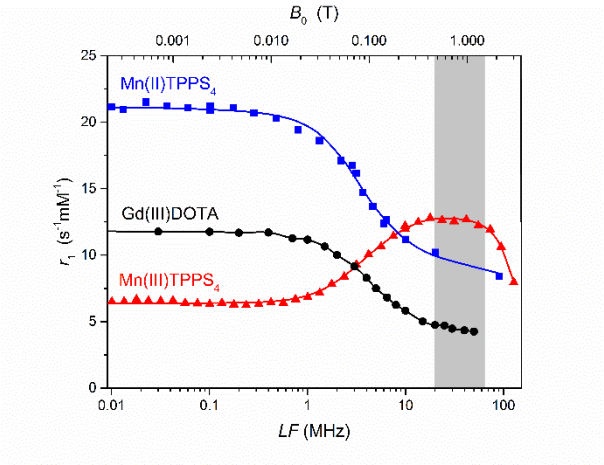


**Fig. 4.** Comparison of the $^1$H NMRD profiles of Mn(II)TPPS$_4$, [Mn(III)TPPS$_4$, and Gd(III)DOTA at 298 K. The plot was constructed with experimental data from ref. [37], [36], and [39], respectively. The shaded region indicates the range of *LF*s at which most clinical MRI machines operate today. The lines are intended only as guides to the eye.

Fitting of NMRD profiles of Mn(III)TPPS$_4$ and other Mn(III) porphyrins with the classical SBM-theory resulted in good fits but with physically unrealistic best-fit parameters [25,29,40,41]. For example, a value of about 2.20 Å for the distance Mn-H$_{water}$ has been obtained from such fittings [25],

which is much too short compared to the Mn-$H_{water}$ distances found in crystal structures (2.77±0.11 Å, see above). It has been suggested that delocalization of the electron spin onto the porphyrin may be the reason for this unusual shape of NMRD profiles of Mn(III) porphyrins [25,29]. However, unrestricted Hartree-Fock calculations have suggested that, in Mn(III)$TPPS_4$, the electron spin is localized on Mn(III) [42]. But on the other hand, a substantial delocalization of the unpaired spin density is supported by spin densities calculated using DFT methods [43–46].

The second-order zero-field splitting (zfs) interaction parameter *D* for Mn(III)$TPPS_4$ has been determined to be -3.16 $cm^{-1}$ by EPR [47]. For such a large *D*-value, the electron spin system will probably be in the vicinity of the zfs limit and then the simple SBM model for the inner-sphere relaxivity is no longer adequate. More complicated models are required to interpret the relaxation data [33,48,49]. Schaefle and Sharp fitted NMRD data of Mn(III)$TPPS_4$ both in water and a polyacrylamide gel with a complex model taking into account the effects of zfs interactions and relatively slow and anisotropic Brownian motion, using as variable parameters the distance Mn-$H_{water}$, different electron spin relaxation correlation times for the $m_S = \pm 1$, and $m_S = \pm 2$ doublet manifolds, and the 4th-order zfs tensor component, $B_4^4$ [33]. All other parameters were fixed at values that were determined independently with other methods. Good fits were obtained for both datasets with a best-fit value of the Mn-$H_{water}$ distance of 2.80 and 2.82 Å for the pre-gelled and gelled sample, respectively (see Fig. 5). These results are in excellent agreement with the distances found in X-ray crystal structures (2.77 Å, see above). The parameter $B_4^4$ appeared to be the principal determinant of the unique shape of the $^1H$ NMRD profile with a local maximum at $B_0 \approx 1$ T. The immobilization of the Mn(III)-complex in the polyacrylamide gel resulted in a significant increase of $r_1$ particularly at the high field part. ($B_0 > 0.1$ T, see Fig. 5).

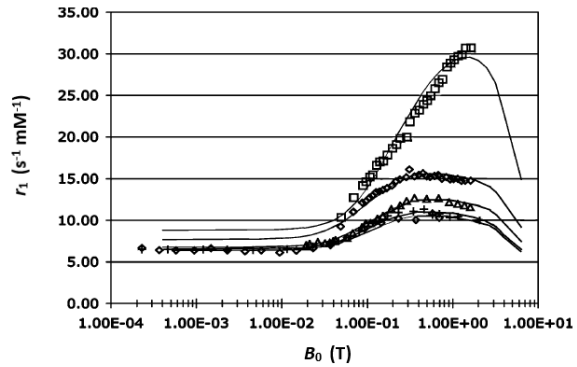


**Fig. 5.** Simulations of Mn(III)$TPPS_4$ $^1H$ NMRD profiles with the use of the model of Schaefle and Sharp [33]. The samples contained, from top to bottom: gelled polyacrylamide (293 K, □), the acrylamide monomer solution prior to gelation (293 K, ◊), and a control sample lacking gel components (pH 8, 293 K, Δ). The experimental data from the latter samples were taken from refs [41] (+) and [40] (◊)

and were measured at 298 K. Reproduced with permission from ref. [33]. Copyright 2005 American Chemical Society.

It seems that only the more complex models, like that of Schaefle and Sharp, can provide a good quantitative description of the spin dynamics of $Mn^{III}$-porphyrin systems. NMRD profiles have been published for a few Mn(III) porphyrin systems [25,36,37,40,41,45,50–56] and usually, no fittings to a model are provided. Many other publications on Mn(III) porphyrins and phthalocyanines report relaxivities measured at only one or two magnetic field strengths. Table 1 compiles these relaxivities and in Fig. 6, reported relaxivities of the porphyrins are plotted as a function of the $^1H$ Larmor frequencies at which they were measured. Because of the large variation in these frequencies, the full NMRD profile of Mn(III)$TPPS_4$ is included in the Fig. 6 for comparison.

**Table 1.** Relaxivities of $Mn^{III}$ -porphyrins and phthalocyanines.

| entry | ligand | $B_0$ (T) | $T$ (K) | $r_1$ ($s^{-1}$ $mM^{-1}$) | $r_2$ ($s^{-1}$ $mM^{-1}$) | Ref. |
|---|---|---|---|---|---|---|
| | *Meso-substituted porphyrins* | | | | | |
| 1 | TCP | 3 | RT | 7.90 | 9.11 | [57,58] |
| 2 | TPP | 1.0 | RT | 12.9 | 17.9 | [59] |
| 3 | TPP in thermosensitive microgel | 3.0 | 298 | 8.4 | | [60] |
| 4 | TPP in thermosensitive microgel | 3.0 | 310 | 14.5 | | [60] |
| 5 | TPP-$mPEG_{550}$ in methylated cyclodextrin-dimer | 3 | RT | 15.69 | | [61] |
| 6 | TPP-$mPEG_{550}$ in methylated cyclodextrin | 3 | RT | 12.64 | | [61] |
| 7 | TPP-2-$OCH_2COO^-$ | 0.47 | RT | 13.0 | 17.2 | [62] |
| 8 | $TF_4PP(mPEG_n)_4$ | 0.94 | 298 | 10.75 | | [51] |
| 9 | *para*-$(TPPS_3)_2$ | 3.0 | RT | 14.1 | 18.0 | [57] |
| 10 | *para*-$(TPPS_3)_2$ | 1.0 | 298 | 20.9 | | [55] |
| 11 | *para*-$(TPPS_3)_2$+ HSA | 1.0 | 298 | 15.8 | | [36] |
| 12 | *meta*-$(TPPS_3)_2$ | 1.0 | 298 | 15.2 | | [36] |

| | | | | | | |
|---|---|---|---|---|---|---|
| 13 | *meta*-$(TPPS_3)_2$ + HSA | 1.0 | 298 | 15.2 | | [36] |
| 14 | $TPPS_4$ | 0.23 | 290 | 10.86 | | [40] |
| 15 | $TPPS_4$ | 0.25 | 310 | 11.0 | | [24] |
| 16 | $TPPS_4$ | 0.25 | 310 | 10.39 | | [27] |
| 17 | $TPPS_4$ | 0.47 | 310 | 10.36 | 12.6 | [23] |
| 18 | $TPPS_4$ | 3 | RT | 7.99 | 9.87 | [63] |
| 19 | $TPPC_4$ | 0.23 | 290 | 10.75 | | [40] |
| 20 | IR825@P(PEGMA-co-APMA)bPMMA@ $TPPC_4$ micelles | 3 | RT | 9.53 | | [64] |
| 21 | PCN-222 ($TPPC_4$-Zr-MOF) | 0.5 | 298 | 30.3 | 36.7 | [65] |
| 22 | PCN-222 ($TPPC_4$-Zr-MOF) | 1.0 | 298 | 35.3 | 52.5 | [65] |
| 23 | $TPPS_3A$ | 0.5 | 310 | 6.7 | | [66] |
| 24 | $TPPS_3A$ | 0.5 | 310 | 11.25 | | [67] |
| 25 | $TPPS_3A$ | 3.0 | RT | 9.33 | 12.0 | [63] |
| 26 | $TPPS_3A$ | 4.7 | 298 | 7.4 | | [68] |
| 27 | $TPPS_3A$-oxidized dextran | 4.7 | 298 | 8.9 | | [68] |
| 28 | $TPPS_3A$-polylactic acid-Dox NPs | 0.5 | 310 | 27.9 | | [66] |
| 29 | $TPPS_3A$-PB61BA | 0.5 | 310 | 19.21 | | [67] |
| 30 | Dox@PLA@Au-PEG-$TPPS_3A$ | 0.5 | 310 | 22.2 | | [69] |
| 31 | $TPPS_3A$ -grafted lipid | 0.5 | 298 | 20.6 | | [70] |
| 32 | $TPP(TMA)_4$ | 0.23 | 290 | 10.97 | | [40] |
| 33 | $TPPC_4$ conjugated with mPEG-$NH_2$ | 11.7 | 303 | 47.7 | | [71] |
| 34 | Amphiphilic TPP deriv. in micelles | 9.4 | RT | 5.0 | | [72] |
| 35 | T4PyP | 0.25 | 310 | 11.53 | | [27] |
| 36 | T4MPyP | 0.23 | 290 | 9.36 | | [40] |

| | | | | | | |
|---|---|---|---|---|---|---|
| 37 | T4MPyP | 0.47 | 310 | 10.6 | | [73] |
| 38 | T2EPyP | 7.0 | 293 | 5.09 | | [74] |
| 39 | T2HexPyP | 7.0 | 293 | 5.34 | | [74] |
| | *Phthalocyanines* | | | | | |
| 40 | PcS | 0.25 | 310 | 10.10 | | [38] |
| 41 | PcS | 0.5 | RT | 7.8 | | [75] |
| 42 | PcS | 7 | RT | 5.12 | | [75] |
| 43 | PcPEG | 0.47 | 298 | 5.7 | | [76] |
| 44 | PcChol | 0.47 | 298 | 4.0 | | [76] |
| | *Pyrrole-substituted porphyrins* | | | | | |
| 45 | PP | 0.23 | 290 | 3.32 | | [40] |
| 46 | PP | 0.47 | 310 | 2.6 | | [73] |
| 47 | PP-poly(L-glutamic acid) | 0.47 | 310 | 6.1 | | [73,77] |
| 48 | PP-poly(L-lysine) | 0.47 | 310 | 7.1 | | [73,77] |
| 49 | PP-poly(L-lysine-L-phenylalanine) | 0.47 | 310 | 9.1 | | [73,77] |
| 50 | PP-poly( L-lysine-L-alanine) | 0.47 | 310 | 3.2 | | [77] |
| 51 | PP included in bialys NPs | 1.5 | 298 | 3.7 | 5.2 | [78,79] |
| 52 | PP in horseradish peroxidase | 2.3 | RT | 7.2 | | [80] |
| 53 | PP in myoglobin | 2.3 | RT | 4.0 | | [80] |
| 54 | PP in heme domain of Thermoanaerobacter tengcongensis | 1.4 | 310 | 12.0 | 16.8 | [81] |
| 55 | PP in cytochrome P450 BM3 | 4.7 | 296 | 2.6 | | [82] |
| 56 | PP in cytochrome P450 BM3 | 1 | 296 | 5.2 | | [82] |
| 57 | P22-xAEMA-PP capsids | 0.45 | 298 | 2.29 | | [83] |
| 58 | P22-xAEMA-PP capsids | 2.1 | 298 | 1.81 | | [83] |

| | | | | | | |
|---|---|---|---|---|---|---|
| 59 | P22-xAEMA-PP capsids | 7.0 | 298 | 1.20 | | [83] |
| 60 | HP-IX in 80 mg $L^{-1}$ BSA | 0.47 | 310 | 6.3 | 8.4 | [84] |
| 61 | BPheoid | 9.4 | RT | 29.1 | | [85] |
| 62 | HPPH-lipid 1 porphysome | 7.0 | RT | 1.2 | 7.0 | [86] |
| 63 | HPPH-lipid 1 disrupted porphysome | 7.0 | RT | 4.0 | 12.9 | [86] |
| 64 | HPPH-lipid 2 (porphysome) | 4.7 | 310 | 0.98 | | [87] |
| 65 | N-HPPH-lipid 2 (porphysome) | 4.7 | 310 | 2.46 | | [87] |
| 66 | Meso | 0.47 | 312 | 1.94 | 2.05 | [88,89] |
| 67 | MSP | 0.23 | 290 | 5.16 | | [40] |
| 68 | CP1 | 0.23 | 290 | 3.53 | | [40] |
| 69 | D24DSA | 0.23 | 290 | 10.03 | | [40] |
| 70 | UROP-1 | 0.23 | RT | 4.8 | | [90] |
| 71 | UROP-1 in serum | 7.0 | 293 | 4.8 | | [90] |
| 72 | BOPP | 0.25 | 298 | 3.60 | | [91] |
| 73 | BOPP | 0.25 | 310 | 4.43 | | [91] |

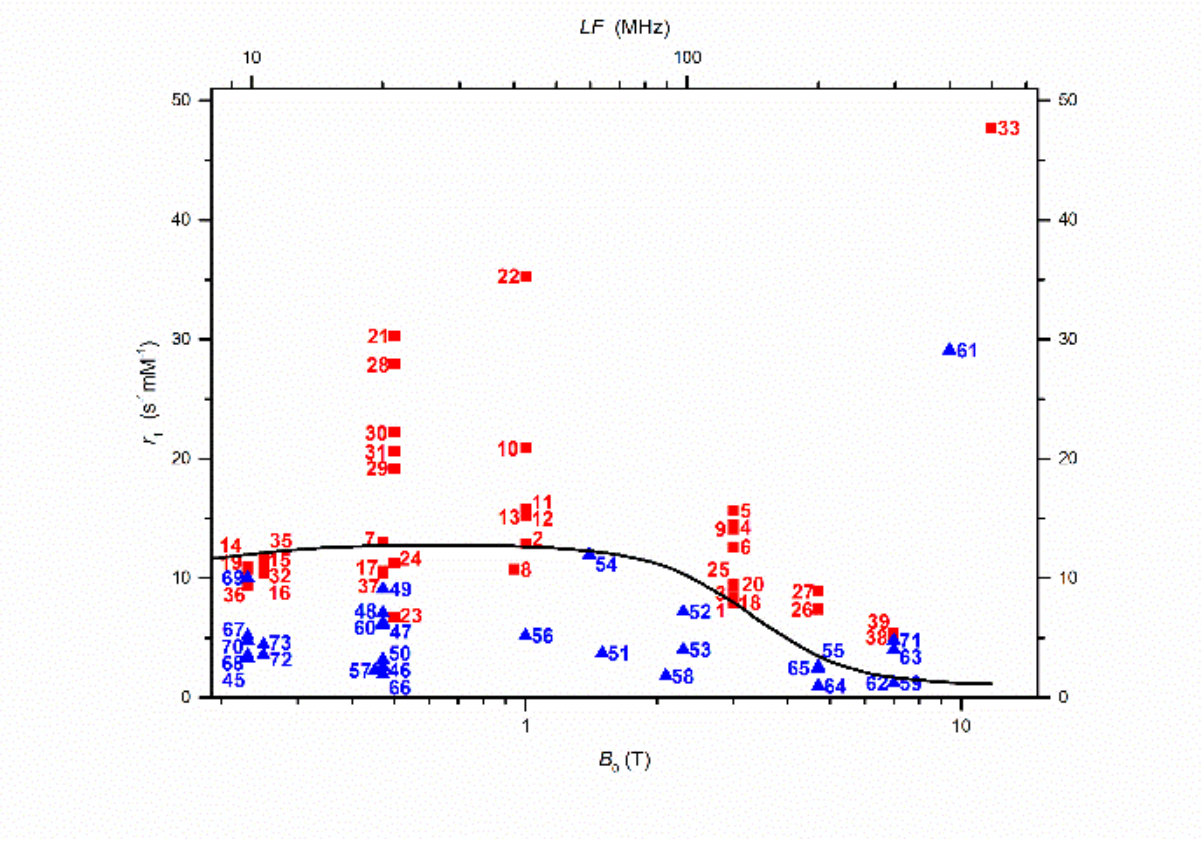


**Fig. 6.** The longitudinal relaxivities of Mn(III)-porphyrins reported in the literature. ■ Meso-substituted Mn(III)porphyrins, ▲ pyrrole-substituted Mn(III)porphyrins. The numbers refer to entries in Table 1. The black curve represents the NMRD profile of Mn(III)TPPS$_4$ at 298 K, constructed with experimental data reported in ref. [36].

*3.2. The effect of self-association and q*

A striking trend in Fig. 6 is that the Mn(III) complexes of pyrrole-substituted porphyrins generally have lower $r_1$ values than Mn(III)TPPS$_4$, while most meso-substituted complexes have approximately equal or higher relaxivities. Kellar and Foster investigated the effect of the addition of acetone-$d_6$ on the NMRD profiles of series of Mn(III) porphyrins with relatively low $r_1$ values in aqueous solution (Mn(III) complexes of MSP, PP, CP1) [40]. It appeared that the $r_1$ values increased up to values that were similar to that of Mn(III)TPPS$_4$, whereas the addition of acetone-$d_6$ to a sample of Mn(III)TPPS$_4$ had almost no effect on its NMRD profile. Since acetone is known to disrupt the self-associates of porphyrins, it may be assumed that the differences in relaxivities are due to the self-association of the Mn(III) complexes of MSP, PP, CP1. The aggregation was confirmed by UV-spectroscopy [40]. It may be accompanied by bridging through the formation of Mn-O-Mn or Mn-(OH)-Mn bridges from the axial water ligands, which results in a reduction of $q$ and since $q$ is linearly proportional to $r_{1,\,IS}$ (see Eq. 1), also to a reduction of $r_1$. Fig. 6 suggests that the Mn(III) complexes of

pyrrole-substituted porphyrins are more prone to aggregation than those of the meso-substituted porphyrins. Possibly steric repulsion among the phenyl substituents blocks the association of the meso-substituted porphyrin complexes. The relatively high $r_1$ of Mn(III)D24DSA ($r_1$ = 10.03 $s^{-1}$ $mM^{-1}$ at 0.23 T and 290 K, see Table 1) [40] may probably be ascribed to the prevention of self-association by Coulomb repulsion due to the 4 negatively charged substituents in this complex. It should be noted that the formation of Mn-O-Mn bridges may also affect the electronic properties of the Mn(III) ions by magnetic coupling.

The Mn(III) complex of tetra sulfonated phthalocyanine (Mn(III)PcS, see Fig. 1) has an $r_1$ value (10.1 $s^{-1}$ $mM^{-1}$ at 0.25 T and 310 K) of the same magnitude as Mn(III)$TPPS_4$ [38,75]. However, Mn(III) complexes of phthalocyanines with four polyethylene glycol chains ($PEG_{500}$) or choline substituents to increase the water-solubility have relatively low $r_1$ values (4-6 $s^{-1}mM^{-1}$ at 0.23 T, 298 K) in comparison to Mn(III)$TPPS_4$ [76].

*3.3. The effect of the water exchange rate ($k_{ex} = \tau_M^{-1}$)*

The water exchange rates of a few Mn(III) porphyrin complexes have been determined from the temperature dependence of $^{17}O$ NMR longitudinal, transverse relaxation rates, and induced chemical shifts [35,73,92,93]. The reported $\tau_M$ values, the activation parameters, and the corresponding $r_1$ values are compiled in Table 2.

**Table 2.** Water residence times and activation parameters in Mn(III) porphyrin complexes

| Complex | pH | $\Delta H^{\ddagger}$ (kJ $mol^{-1}$) | $\Delta S^{\ddagger}$ (J $mol^{-1}$ $K^{-1}$) | $\tau_M^{298}$ (ns) | $r_1$ ($s^{-1}$ $mM^{-1}$) | ref |
|---|---|---|---|---|---|---|
| Mn(III)$TPPS_4$ | 6.0 | 54 | +79 | 37 | 10.4[a] | [35] |
| Mn(III)T2EPyP | 6.0 | 36 | +4 | 243 | 5.1[b] | [35] |
| Mn(III)T2HexPyP | 6.0 | 34 | -2 | 175 | 5.3[b] | [35] |
| Mn(III)$T_4$MPyP | 5.5 | 33.22 | +13.47 | 21.4 | 10.6[c] | [40] |
| Mn(III)PP | 5.5 | 21.05 | -34.10 | 47.4 | 2.6[c] | [40] |
| Mn(III)PP-PGA | 5.5 | 29.92 | -10.96 | 104 | 6.1[c] | [40] |
| Mn(III)$TPPS_4$ | 2 | 32.7 | +1.65 | 71 | 10.4[a] | [93] |
| Mn(III)$T_4$MPyP | 2 | 40.7 | +45.3 | 100 | 10.6[c] | [93] |

[a] At 310 K and 0.41 T, ref. [23]; [b]at 293 K and 7 T, ref. [74]; At 310 K and 0.47 T

Although the ionic radius of Mn(III) is smaller than of Gd(III), the order of magnitude of the $\tau_M$-values are comparable with most Gd(III) complexes [2,3,94]. This high lability of the axially bound

water can be explained by the *cis*-effect of the hydrophobic porphyrin unit and by the Jahn-Teller distortion in the $d^4$ high-spin electronic configuration of Mn(III). The relatively high positive $\Delta S^{\ddagger}$ for Mn(III)$TPPS_4$ suggests that a dissociative interchange mechanism ($I_d$) is operative here. The positively charged *ortho*-substituents in Mn(III)T2EpyP and Mn(III)T2HexPyP reduce the water exchange rates by an order of magnitude and seem to shift the mechanism towards interchange (*I*), but if the charges are located at the *para*-position the effect is rather small. High-pressure NMR measurements of the activation volumes for Mn(III)$TPPS_4$ at pH 2 gave small positive values (2.9 $cm^3$ $mol^{-1}$), supporting that a dissociative interchange mechanism ($I_d$) is operative [35]. Anyway, the $\tau_M$-values are all long compared with $\tau_S$ and short compared with $T_{1M}$ and therefore, they most likely do not influence the relaxivities of these complexes.

*3.4. The electronic effect of substituents*

It may be expected that the distribution of the spin density and the molecular electronic potential in the porphyrin backbone are affected by electron-withdrawing or donating effects of substituents and that this is reflected in the parameters governing the relaxivity [43–45]. Bryant et al. have attempted to demonstrate this by investigating the effect of hexa-bromination (in the $\beta$-pyrrole positions) of $TPPS_4$ on the NMRD profiles of the Mn(III) complex [41]. A significant increase in $r_1$ was observed (6.3 $\rightarrow$ 8.5 $s^{-1}mM^{-1}$) at the low-field region (*LF* < 0.2 MHz) of the NMRD profile, which was suggested to be due to a dominant contribution of spin delocalization. An undesirable side effect of the electron-withdrawal by the Br-atoms was the destabilization of the porphyrin complex resulting in leaching of Mn(III).

For Gd(III)-complexes, lowering the symmetry results in a decrease in $r_1$ in the low-field region of NMRD profiles caused by a reduction in the electronic relaxation time [95–97]. An inspection of the low field regions of published NMRD profiles of Mn(III) porphyrins with $q = 2$ shows a similar phenomenon [25,36,55,56,37,40,41,45,50,51,53,54]. Most of these NMRD profiles concern compounds with $C_4$-symmetry and have low-field (*LF* < 0.2 MHz) $r_1$-values around 6.5 $s^{-1}mM^{-1}$, whereas less symmetric compounds have at least 20% lower $r_1$-values in the flat low field part of their NMRD profiles. However, it is unclear whether this trend continues at the higher field strengths, which are of relevance for clinical MRI diagnostics.

*3.5. The effect of molecular mobility ($\tau_R$)*

Fig. 6 suggests that reduction of mobility is an important tool to increase the $r_1$ of Mn(III) porphyrin-based MRI CAs at the clinical most interesting magnetic field strengths (0.5-1.5 T). Most of

the data points in Fig. 6 that are located above the profile of Mn(III)TPPS$_4$ (the black curve) represent Mn(III) porphyrins with reduced mobility, achieved *via* several methods.

*3.5.1. Heme proteins with Mn(III) substituting the natural metal ion in the porphyrins*

Several natural metalloproteins containing a Fe(III)PP or Fe(III)HP-IX domain have been modified by replacing the native Fe(III) by Mn(III); horseradish peroxidase and myoglobin by classical chemical strategies [80] and more recently, cytochrome P450 BM3 [82] and the nitric oxide/oxygen-binding protein from Thermoanaerobacter tengcongensis [81] by protein engineering techniques. Generally, the substitution led to an increase of the $r_1$ value, because Fe(III) occurs predominantly in the low spin state ($S$ = ½), whereas Mn(III) is in the high spin ($S$ = 2) state, but the values did not exceed those of free Mn(III)PP in the monomeric state (see Table 1, entries 45, 52-56). In these proteins, the self-association is impossible but $q$ probably does not reach a value of 2 because the axial sites at Mn(III) are coordinated to amino acids or not accessible to water for steric reasons. An exception is Mn(III)PP included in the heme Nitric oxide/OXygen binding (H-NOX) domain from Thermoanaerobacter tengcongensis (Table 1, entry 54), which had relatively high relaxivities, probably thanks to structural perturbations increasing the water accessibility of the paramagnetic center or to an increase of $q$ and the beneficial effect of an increase in $\tau_R$ [81]. The X-ray structure of this compound showed that one of the axial positions is occupied by a histidine.

*3.5.2. Mn(III) porphyrins covalently bound to large size compounds*

Covalent attachment of the Mn(III) complex of protoporphyrin (Mn(III)PP) to polylysine and copolymers of lysine and some other amino acids resulted only in a modest increase in relaxivity compared to free Mn(III)PP ($r_1$ = 2.6 $s^{-1}$ $mM^{-1}$ at 0.47 T and 37 °C); the $r_1$ values of the conjugates were found to be in the range 3.2-7.1 $s^{-1}$ $mM^{-1}$ (see Table 1, entries 46-50) under the same conditions [73,77]. Fluorescence depolarization measurements indicated that the conjugates have dynamic characteristics very similar to free Mn(III)PP and therefore, $\tau_R$ of the conjugates is probably determined by the local mobilities of the Mn(III)PP units. The modest increase in $r_1$ observed upon conjugation can be attributed to the disruption of the self-aggregation. Maybe, coordination of the axial sites of Mn(III) by lysine amino groups contributes to the disappointing increase in $r_1$. Since multiple Mn(III) porphyrins are bound to each (co)polymer molecule, this may be a useful approach for the design of targeted CAs, since each polymer molecule can deliver a large amount of paramagnetic Mn(III) ions to the sites of interest. Conjugation of Mn(III)TPPS$_3$A ($r_1$ = 7.4 $s^{-1}$ $mM^{-1}$ at 4.7 T) to oxidized dextran also resulted only in a small increase in relaxivity (to $r_1$ = 8.9. $s^{-1}$ $mM^{-1}$ at 4.7 T [68] but it should be noted that the effect of an increase of $\tau_R$ at this relatively high magnetic field

strength may be expected to be relatively small. An investigation with a cancer cell line showed that this CA accumulates at the cell membrane.

By contrast, linking of Mn(III)TPPS$_3$A to the surface of polylactic acid (PLA) NPs, (diameter 99 nm; $r_1$ = 27.9 $s^{-1}$ $mM^{-1}$ at 0.5 T and 310 K) [66] or to a fullerene ([6,6]-phenyl-$C_{61}$-butyric acid) gave conjugates with much higher $r_1$ (19.2 $s^{-1}$ $mM^{-1}$ at 0.5 T and 300 K) [67]. Apparently, the local mobility in the latter two systems is more effectively reduced. High relaxivities were also reported for Mn(III)TPPS$_3$A attached to the surface of other NPs. A theranostic system fabricated by the formation of an Au nanoshell around PLA NPs entrapping the chemotherapeutic doxorubicin (DOX), followed by covalently attaching Mn(III)TPPS$_3$A to the Au shell surface through a PEG linker resulted in a system (DOX@PLA@Au-PEG-TPPS$_3$A) with a diameter of 124 nm and $r_1$ = 22.2 $s^{-1}$ $mM^{-1}$ at 0.5 T and 310 K [69].

Surprisingly high $r_1$-values (47.7 $s^{-1}$ $mM^{-1}$ at 11.7 T and 303 K) were obtained for Mn(III)TPPC$_4$ conjugated through amide bonds with four mPEG tails (molecular weight 2.3 kDa) [71]. The large relaxivity, which is rather unexpected for such a high magnetic field strength, was attributed to a reduction of the molecular tumbling. It was shown that the four PEG chains can wrap the porphyrin plane. Possibly, the hydrophilic PEG chains keep exchangeable protons and water molecules nearby the paramagnetic center with favorable residence times.

An efficient approach of increasing relaxivities through an increase of $\tau_R$ is by dimerization. The advantage is that the increase in $\tau_R$ is accompanied by a doubling of the number of Mn(III) ions per molecule. Dimers have been obtained by connecting two MnTPPS$_3$ molecules through either the *meta*- or *para*-carbon atoms of the non-sulfonated phenyl groups to give *meta*-(Mn(III)TPPS$_3$)$_2$ and *para*-(Mn(III)TPPS$_3$)$_2$, respectively [36,56]. An additional advantage of the phenyl-phenyl bridge is its restricted mobility. *Para*-(Mn(III)TPPS$_3$)$_2$ appears to have the highest relaxivity (20.9 $s^{-1}mM^{-1}$, see Table 1, entries 9,10,12) likely due to a difference in molecular volume. Experiments with rats have shown that these CAs exhibit hepatic clearance in contrast to the more polar Mn(III)TCP, which has a rapid renal clearance at a rate comparable to Gd-DTPA [56]. Very recently, a study on somewhat similar dimers and trimers was reported [52]. The connection between the monomeric units was not directly between two phenyl groups but through a thiourea linker. These oligomers had somewhat lower $r_1$ values ($r_1$ = 17-20 $s^{-1}$ $mM^{-1}$ at 1 T and 298 K) probably due to higher local mobility of the linkers between the monomeric units.

*3.5.2. Mn(III) porphyrins non-covalently bound to large size compounds*

A study of the interaction of Mn(III)TPPS$_4$ with BSA shows that the $r_1$ of Mn(III)TPPS$_4$ in the presence of bovine serum albumin (BSA) is at 4.9 T and 296 K more than twice as high as in the absence of BSA, up to about an equimolar molar ratio $Mn^{III}$TPPS/BSA, probably due to an increase of $\tau_R$ upon binding of the Mn(III)-complex [98,99]. With an excess of Mn(III)TPPS$_4$, $r_1$ drops to ultimately the value for free Mn(III)TPPS$_4$ suggesting that upon further increase of the molar ratio Mn(III)TPPS$_4$/BSA, the Mn(III)TPPS$_4$ on the BSA dimerizes on the surface to an aggregate with negligible relaxivity, which has been ascribed to an antiferromagnetic coupling between the neighboring Mn(III)-ions and a decrease in $q$.

In the presence of 0.67 mM HSA, the $r_1$ of Mn(III)TPPC$_4$ conjugated with four PEG tails (see above) was even higher by a factor of 1.3, probably due to a non-covalent interaction between the CA and HSA [71]. Such an increase was not observed with Mn(III)TPPS$_4$.

Sur *et al*. have investigated host-guest interactions between cyclodextrins (CDs) and MnTPPS$_4$ [53]. The strongest interaction occurs with β-CD; in the presence of a 10-fold excess of this CD, 30% increase in $r_1$ was observed for Mn(III)TPPS$_4$ at 0.47 T and 298 K. From an inspection of molecular models, it was concluded that only two out of the four phenyl groups of Mn(III)TPPS$_4$ can be encapsulated by β-CD. Sun *et al.* have included a mPEGylated derivative of Mn(III)TPP into a bridged bis(permethyl-β-CD) (see Fig.7) [61]. A polymeric inclusion compound was formed, whereas a mono-β-CD gave a 1:2 Mn(III)TPP-CD inclusion compound. The relaxivities of these inclusion compounds at 3 T and RT were somewhat lower than those of the non-included compounds (see Table 1, entry 5,6). Probably the water access in the CDs is somewhat hindered and counteracting an increase in $r_1$ due to the larger $\tau_R$.

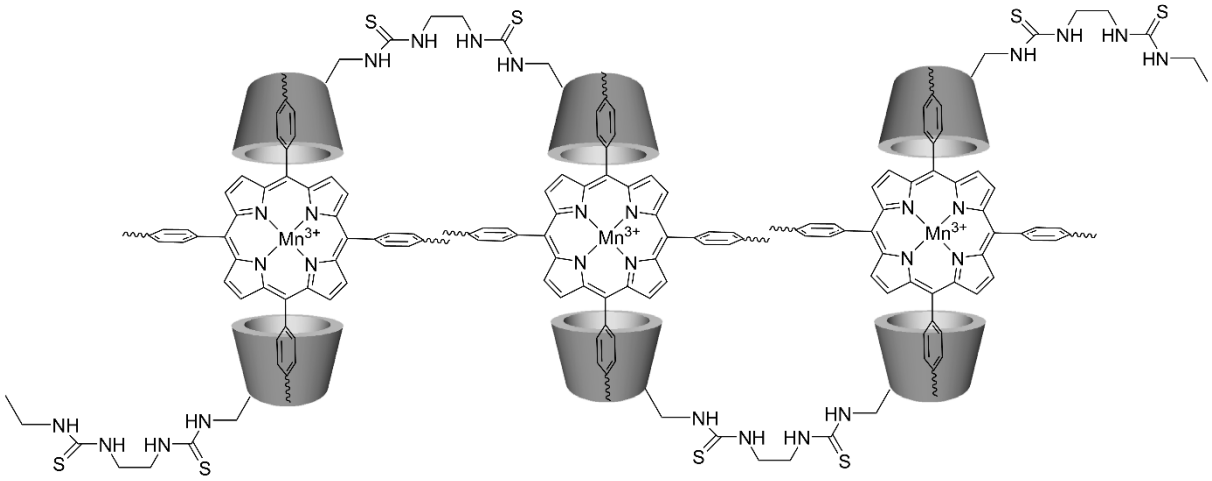

**Fig. 7.** Schematic representation of the polymeric inclusion compound formed from a bridged permethylated β-CD (the cones in the Figure) and mPEGylated Mn(III)TPP.

The above discussed dimeric porphyrin derivative *para*-(Mn(III)$TPPS_3$)$_2$ binds tightly to HSA through the biphenyl bridge ($K_d$ = 0.23 ± 0.03 μM ) and *in vivo* studies in rats have shown that it has a long retention time in blood. Therefore, it has potential as a blood pool agent [55,57]. However, the HSA binding is accompanied by a decrease in $r_1$ (from 20.9 to 16.8 $s^{-1}mM^{-1}$ at 1 T and 298 K) rather than an increase as would be expected. The UV spectrum of the dimeric agent *para*-(Mn(III)$TPPS_3$)$_2$ suggests that there is little or no electronic interaction among the two Mn-porphyrin units of the dimer. Possibly, the *para*-(Mn(III)$TPPS_3$)$_2$ is buried deeply in the HSA pocket, which reduces *q* and thus $r_1$ [55]. The isomeric compound *meta*-(Mn(III)$TPPS_3$)$_2$, in which the bridging phenyl groups are connected through their *meta*-C-atoms, has a twisted shape and a lower molecular volume. Accordingly, it has a lower $r_1$ at about 1 T. The non-covalent binding of this compound with HSA is weaker ($K_d$ = 16.5 μM) in comparison to *para*-(Mn(III)$TPPS_3$)$_2$, as a result, both isomers have about the same $r_1$ at about 1 T in the presence of HSA [36].

*3.5.3. Mn(III) porphyrins included in micelles, liposomes, and virus capsids*

Hydrophobic porphyrins have been converted into amphiphilic compounds that self-assembled to soft NPs (micelles, or liposomes). Micelles formed by an amphiphilic PEG-dendron derivative of 5,15-diphenylporhyrin [72] had a much lower relaxivity ($r_1$ = 5.0 $s^{-1}$ $mM^{-1}$ at 9.4 T) than for example, the above-described Mn(III)$TPPC_4$ conjugated through amide bonds with four mPEG tails. The somewhat disappointing relaxivity may be due to high local mobility in the micelles. Higher $r_1$ values (9.53 $s^{-1}mM^{-1}$ at 3 T) were obtained by self-assembly of the amphiphilic block copolymer (P(PEGMA-co-APMA)-b-PMMA) (see below) [64]. In that system, the higher relaxivity is most likely due to reduced mobility thanks to cross-linking of the amphiphilic chains.

Porphysomes, liposome-like NPs (~100 nm diameter), are constructed by self-assembly of porphyrin lipids (see below). The porphyrin packing density per particle is high (>80 000 per particle). They have also lower relaxivities than free porphyrin-peptide conjugates as is witnessed by an increase in relaxivities upon disruption of the supramolecular structure by a detergent ($r_1$: 1.2 → 4.0 $s^{-1}$ $mM^{-1}$; $r_2$: 7.0 → 12.9 $s^{-1}$ $mM^{-1}$) [86]. The relatively low relaxivities in the liposomes have been ascribed to the limited water access to the $Mn^{III}$ cations in the bilayer. These systems can be applied in MRI-guided photothermal therapy (see below).

Liposome-like porphysome nanovesicles have also been constructed with the Mn(III)HPPH-lipid and Mn(III)N-HPPH-lipid included in the bilayer [87]. Molecular dynamics calculations suggested

that the latter conjugate had a relatively high amount of water contained in the hydrophobic bilayer. Correspondingly, the relaxivity of the Mn(III)N-HPPH-lipid nanovesicles ($r_1$ = 2.46 $s^{-1}$ $mM^{-1}$) was higher than of Mn(III)HPPH-lipid (0.98 $s^{-1}$ $mM^{-1}$). It was suggested that this is rationalized by the formation of water networks inside the Mn(III)N-HPPH-lipid nanovesicles.

Pan *et al*. have included Mn(III)PP in toroidal-shaped NPs (190 nm diameter, Mn(III)-nanobialys) prepared by self-assembly from an amphiphilic conjugate of branched polyethyleneimine (MW – 10 kDa) and linoleic acid [100,101]. The relaxivities were rather high ($r_1$ = 3.7 $s^{-1}$ $mM^{-1}$ at 1.5 T and 298 K), suggesting that the Mn(III)PP chelates are readily accessible for water molecules, although the effect of immobilization seems to be negligible. Since each NP contained about 165,000 Mn(III)- ions, these systems are very suitable for targeting, which was demonstrated for fibrinogen clots after attaching biotin as a targeting vector. The NPs have also potential as theranostics (see below).

Various loadings of Mn(III)PP (90 to 3,646 molecules *per* capsid) have been covalently attached to a cross-linked polymer synthesized from aminoethyl methacrylate and N,N'-methylenebisacrylamide (x-AEA) inside the cavity of bacteriophage P22 virus capsid (P22-xAMEA-Mn(III)PP) [83]. The $r_1$ values of these loaded capsids were almost independent of the degree of loading and about equal to that of free Mn(III)PP (1.5-3.7 $s^{-1}$ $mM^{-1}$ at 2.1 T and 298 K), but obviously, the relaxivities *per* particle here and also in the other soft NPs discussed above are impressive [83]. The $r_1$ values increase substantially upon the addition of 20 % acetone-$d_6$, which suggests that interaction between the Mn(III)PP units inside the capsid is responsible for the low $r_1$ values as compared to free Mn(III)PP. It should be noted that NPs with Mn(III) porphyrin complexes at the outer surface have much higher $r_1$ values (see above). Surprisingly, $r_2$ of these capsids decreases with the degree of loading with Mn(III)PP. Possibly, this is caused by antiferromagnetic coupling between neighboring Mn(III) cations inside the capsid [83].

*3.5.4. Mn(III) porphyrins included in hard nanoparticles*

Very high relaxivity ($r_1$ = 35.3 $s^{-1}mM^{-1}$ at 1 T and 298 K) was exhibited by a nanoparticulate metal-organic framework (NMOF) that was constructed by self-assembly of Mn(III)TPP$C_4$ ligands and eight-connected bio-compatible $Zr_6$ clusters (PCN-222) [65]. The high $r_1$ can be attributed to the open network structure of the MOF with channels (pore size 1.25 nm) having a high affinity and good access of water to Mn(III), while the mobility is optimally reduced. In another approach, the Zr in the NMOF (diameter 265 nm) was attached to S-nitrothiol functions [102]. The $r_1$ of this material was 26.9 at 1.2 T. Both MOF materials have potential as theranostic (see section 7).

**4. Biodistribution, pharmacokinetics and toxicity**

Much research has been carried out on the synthesis, structural characterization, physical, and biological properties of Mn(III) porphyrin derivatives aiming at using them as MRI CAs. Very promising data have been obtained by design improvements of the ligand structure. However, concerns regarding the *in vivo* biodistribution, pharmacokinetics (PK), and toxicity of these compounds are limiting their translation into clinical studies. A brief overview of experimental results on these properties with cells and animal models is reported here, as well as an attempt to correlate structural and biological properties. These properties are essential in determining their prospects for diagnostic clinical application.

Because Mn(III) porphyrin complexes tend to localize in tumors, the biodistribution and PK of Mn(III) porphyrin complexes have often been studied using dynamic contrast-enhanced (DCE) MRI of animal tumor models. Mn(III)$TPPS_4$ was the first Mn(III) porphyrin considered as a potential alternative to Gd-based MRI CAs, and it is the most investigated one, including *in vitro* and *in vivo* studies with different animal models.

Mn(III)$TPPS_4$ was tested in athymic mice bearing subcutaneous human colon carcinoma xenografts. After i.v. injection, $T_1$-weighted MRI images showed, initially, enhanced contrast in blood and various tissues (kidney, tumor, liver, muscle) due to the local increase of $R_1$ of water protons. However, the compound rapidly cleared from the blood and concentrated in those organs, followed by a decrease of contrast in the kidney and liver and a final increase in the tumor. At the highest dose used, a maximum contrast in the tumor was reached after 4 days [14,18]. Another study with mice bearing L1210 solid tumors showed that Mn(III)$TPPS_4$ had a biodistribution and PK similar to the tumor model previously mentioned, and was a tumor-specific MRI CA. $T_1$-weighted MRI images at a 0.15 T clinical scanner showed an enhancement in the contrast between the tumor and adjacent tissue with an $R_1$ value in the L1210 tumor proportional to the concentration of Mn(III)$TPPS_4$ administered and the time intervals between the injection and analysis. Relatively high intensity ratios of tumor to normal tissues were obtained (e.g. > 90 for tumor/muscle), with preferential renal excretion [24]. The effect of Mn(III)$TPPS_4$ as MRI CA was also evaluated in experimental rat brain tumors. Cells from the glioma cell line F98 were inoculated in the animal brain, and after some days to grow the tumor, Mn(III)$TPPS_4$ was i.p. injected (0.25 mmol $kg^{-1}$). After four days, the contrast between tumor and peritumoral tissue was strongly enhanced in $T_1$-weighted images [103]. The Mn(III)-tetra-sulfonated phthalocyanine ($MnPcS_4$, Fig. 1) was also found to be a potential tumor-selective contrast agent in MRI, with relaxivity higher than Gd-DTPA and similar to Mn(III)$TPPS_4$, and liver retention longer than for Mn(III)$TPPS_4$ [38].

Ni et al. observed with 0.05 mmol $kg^{-1}$ Mn(III)TPP(3CM)$_4$ that liver tumors showed contrast enhancement one time after 5 min (analog to non-specific interaction) but at other times only after a delay of more than 3 h [62]. An MR imaging-microangiography-histology matching technique revealed that the latter compartments were non-viable components, including necrosis (n = 10), thrombosis (n = 7), and cystic secretion (n = 3), but not viable tumor tissue. This has been exploited to visualize necrosis in acute myocardial infarction [59,104].

Substituents on the Mn(III) porphyrin determine to a large extent the biodistribution and the excretion; size and polarity are important parameters. This is nicely demonstrated by Cheng et al., who monitored the pharmacokinetics by whole-body MRI of healthy mice after administration of 0.05 mmol $kg^{-1}$ of GdDTPA, Mn(III)TCP, Mn(III)TPPS$_4$, or *para*-(Mn(III)TPPS$_3$)$_2$ (see Fig. 8) [56,57]. With the smallest CAs, GdDTPA and Mn(III)TCP, the kidney lights up in the images within 10 min, soon after followed by the bladder, and the contrast enhancement fully disappears after 24 h, suggesting very rapid renal clearing. The somewhat larger Mn(III)TPPS$_4$ gives initially enhancement of kidney and bladder, but after some time also of the liver. This agent shows both renal and hepatic clearance. With the dimeric agent, *para*-(Mn(III)TPPS$_3$)$_2$, the intensity of the bladder does not increase after the injection of the CA, but the intensity of the cardiovascular system is greatly and long-lasting enhanced, which shows that it is a blood pool agent. Analysis of the urine confirmed the above conclusions regarding the clearance.

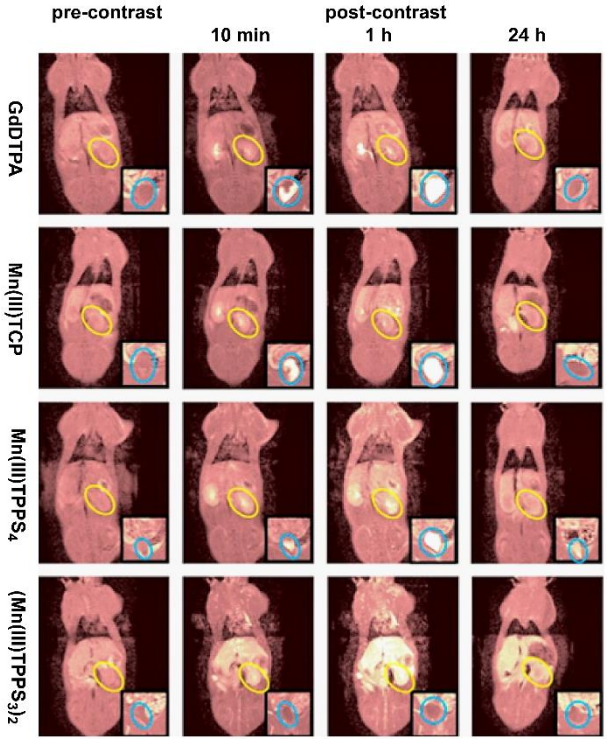

**Fig. 8.** $T_1$-weighted whole-body MRIs of rats at 3 T. The location of the left kidney is highlighted in the yellow circle, while that of the bladder, from separate bladder MRI slices, is delineated within the blue circle. Copied with permission from Ref. [56]. Copyright 2014 American Chemical Society.

Aiming at improving the biological properties of Mn(III)$TPPS_4$, chemical changes were made to the porphyrin moiety. The size, charge, acid/base properties, lipophilicity, and hydrophilicity have been modified to tune the complex for optimal performance. $MnTPPS_3A$ was synthesized and its $T_1$ contrast enhancement capacity was compared with that of $MnTPPS_4$ in an *in vitro* study using several clinical subtypes of breast cancer cells, at 3.0 T. It was shown that $MnTPPS_3A$ gave the highest positive contrast. Both Mn-porphyrin complexes, at non-toxic concentrations, are significantly more sensitive to detect breast cancer cells than Gd-DTPA, due to their higher tumor cell uptake and higher relativity [63].

Following the same ligand design strategy to change chemical properties (hydrophilicity and lipophilicity) of the compounds, studies with other tumor-seeking Mn(III)-porphyrins presenting different lipophilicities were carried out by DCE MRI. The lipid-soluble Mn(III)Meso (Fig. 2) can cross the blood brain barrier (BBB). After i.v injection in a rat with a brain glioma, $T_1$-weighted images showed an enhancement of both the tumor and normal hepatic tissue. This CA is rapidly excreted through the biliary system [89]. *In vivo* experiments in normal Sprague-Dowley rats injected with a water-soluble cationic complex prepared by amidation of Mn(III)$TPPC_4$ with 2-amino-1,3-propanediol showed significant MRI positive contrast in the heart, liver, lungs, and gastrointestinal tract, with long retention in the liver, but suffered from acute toxicity ($LD_{50}$ = 0.1 mmol $kg^{-1}$, see later) [54]. The Mn(III)-HOP-8P complex (HOP-8P = HP-IX endowed with phenylethyl substituents at the hydroxyl functions and with the carboxylate functions amidated with aspartic acid) contains a side-chain combination that confers amphiphilic properties to the complex, allowing a higher concentration in tumors. Its potential as a tumor-specific MRI CA was evaluated in the tumor-bearing SCC-VII mouse model, at 1.5 T. During 24 h after i.v. injection of the CA, the MRI images showed tumor enhancement. The CA was cleared from the circulation, liver, kidneys, and muscle, in the 24 h following administration of 0.1 mmol CA $kg^{-1}$, but was progressively accumulated within the tumor, presenting a wider imaging window than other compounds and no severe toxic effects. Although no detailed PK and toxicity data were reported, this Mn(III) porphyrin might be a promising theranostic for the monitoring of photodynamic, neutron capture, and radiation therapeutic effects of Mn(III)-porphyrins [105,106]. Later, a histopathologic correlation revealed that both necrotic and viable tissue were enhanced but with different enhancement patterns [107].

Mn(III)$T2EPyP^{5+}$ and Mn(III)$T2HexPyP^{5+}$ (Fig. 1), which already demonstrated to be antineoplastic SOD mimics, peroxynitrite scavengers, and cell redox signaling modulators, were also

investigated as MRI CAs for prostate cancer imaging (at 7.0 T), using C57 black mice implanted with RM-9 prostate cancer cells on the hind limb. Both CAs were i.p. injected 90 min before image acquisition and notorious positive tumor/background contrast ratios were observed, which was greatest for Mn(III)T2EPyP$^{5+}$ due to its higher tumor accumulation, although the $R_1$ value was higher for Mn(III)T2HexPyP$^{5+}$. The detection limit observable for such contrast was in the low µM range, which is 1-2 orders of magnitude lower than for the clinical small Gd-based MRI CAs, which is a great advantage [21,74].

Recently, Mn(III)-chelated porphyrin microbubbles (MnP-MBs) have been prepared by self-assembly of an Mn(III)-chelated porphyrin lipid encapsulated in perfluoropropane gas. Upon i.v. injection of the MnP-MBs into U87 glioblastoma tumor-bearing nude mice, an enhanced ultrasound (US) imaging capacity of these structures was observed. Local tumor US disruption converts MnP-MBs into nanoparticles *in situ*, leading to tumor MRI contrast enhancement within 30 min at the very low Mn injection dose of 0.09 mg (1.65 µmol kg$^{-1}$), demonstrating to be an efficient US/MRI bimodal tumor CA [108].

Comprehensive biodistribution and PK studies using conventional methods have been reported on a series of positively charged Mn(III) porphyrins (the hydrophilic Mn(III)T2EPyP$^{5+}$ and Mn(III)T2MPyP$^{5+}$, and the lipophilic Mn(III)T2BuPyP$^{5+}$, Mn(III)T2HexPyP$^{5+}$, and Mn(III)T2BuOEPyP$^{5+}$, see Fig. 1) in different organisms using different administration modes [109]. The obtained data showed that these complexes accumulated up to 10-fold more in tumor than in normal tissue and distributed in all organs and cellular organelles explored. The biodistribution of these Mn(III) porphyrins was related to their lipophilicity. The highest levels of Mn(III) porphyrins were found in the liver and kidneys (at µM levels), and the lowest in the brain (at nM levels). The lipophilic and cationic, Mn(III)T2HexPyP$^{5+}$ and Mn(III)T2BuOEPyP$^{5+}$ accumulated several-fold more in the brain than the hydrophilic Mn(III)T2EPyP$^{5+}$, indicating a more efficient BBB crossing of the former one. The complex Mn(III)T2BuOEPyP$^{5+}$ was shown to have lower toxicity, reduced liver accumulation, and slightly reduced brain accumulation compared to the more lipophilic Mn(III)T2HexPyP$^{5+}$. The penetration of these Mn(III) porphyrins into cellular organelles was also investigated. All the cationic Mn(III) porphyrins accumulated more in the nucleus than in the cytosol of macrophages due to their high positive charge, and their binding to membranes, lysosomes, and the endoplasmatic reticulum of adenocarcinoma cells. The latter is favored because of the presence of anionic phospholipids in these organelles. At high levels, these Mn(III) porphyrins can damage membranes and be toxic. All these Mn(III) porphyrins showed preferential accumulation in mitochondria relative to the cytosol. *In vivo* studies indicated that the most hydrophilic compound (Mn(III)T2EPyP$^{5+}$) accumulates in heart mitochondria with a mitochondria/cytosol ratio of 1.6:1, whereas this ratio increases to 3:1 for the more lipophilic MnT2BuOEPyP$^{5+}$ and MnT2HexPyP$^{5+}$. In a mouse brain, this ratio was 1:0.5 for

MnT2BuOEPyP$^{5+}$ and MnT2HexPyP$^{5+}$, whereas MnT2EPyP$^{5+}$ was not found in mouse brain mitochondria. These data show that Mn(III) porphyrins with high cationic charge and high lipophilicity of the pyridyl alkyl chains favor mitochondrial accumulation [21,109].

Free Mn cations are considerably less toxic than Gd ions. In the blood of healthy humans, the Mn-concentration ranges from 4 to 15 μg $L^{-1}$, but overexposure to Mn is neurotoxic and may lead to Parkinson-like symptoms [110]. Porphyrin is an ideal ligand for the sequestering of Mn(III) because that ion fits perfectly in the cavity of the $N_4$-site. This is demonstrated by the fact that dissociation could not be detected 9 days after the dissolution of Mn(III)TPPS$_4$ in human serum [18]. Mn (III)TCP has been shown by UV-Vis, HPLC, and NMRD to be kinetically inert for more than a month at pH 2-7 and 310 K, including when challenged with competing endogenous metal cations [111]. Moreover, urine collected during *in vivo* experiments with rats did not contain metal-free porphyrins.

While most of the requirements to obtain therapeutic Mn-porphyrin complexes with acceptable redox properties have been met, it remains a challenge to minimize their toxicity. Features such as lipophilicity, polarity, and hindered cationic charge can affect their interaction with biological molecules and cause various toxic effects. Many studies on the cytotoxicity of Mn(III) porphyrins have been reported. Here we focus on *in vivo* toxicity and safety studies with animal models.

The toxicity of Mn(III) porphyrin complexes at doses required for sufficient MRI contrast (usually the lowest detection limit is between 5 and 50 μmol $kg^{-1}$) might be of some concern. No acute toxic effects have been reported on MRI studies in which Mn(III)TPPS$_4$ was intravenously injected into mice at doses lower than 0.38 mmol $kg^{-1}$. Such doses are somewhat lower than the $LD_{50}$ for mice (0.51 mmol $kg^{-1}$) [18,112]. The $LD_{50}$ for Mn(III)PcS is in the same range (0.72 mmol $kg^{-1}$) [38]. It should be noted that often temporary greenish or brownish discoloration of the skin has been observed after i.v. administration of Mn(III) porphyrin CAs [113].

The more lipophilic pyrrole substituted porphyrins like Mn(III)PP and Mn(III)UROP-1 are more toxic and have $LD_{50}$ values of 0.19 and 0.18 mmol $kg^{-1}$, respectively [90,114]. Also, when the hydrophilic water-soluble Mn(III) complexes of TPPC$_4$ amidated with amino-propanediols were injected into Sprague-Dowley rats at a dose of 0.1 mmol $kg^{-1}$, acute toxicity was observed, showing that this dose is too high for clinical use. As monitored by $T_1$-weighted MRI images, this effect is a consequence of too long retention in the liver, after its accumulation in the heart, liver, lungs, and gastrointestinal tract [54].

After extensive *in vivo* safety and toxicity studies using animal models, the radioprotective and cancer therapeutic properties of some positively charged tetrakis(N- alkyl-pyridinium-2-yl)-substituted Mn(III)-porphyrins led to clinical trials in humans for the radioprotection of various organs, such as brain and neck [21,115]. After i.v. administration of Mn(III)T2EPyP$^{5+}$ (Fig. 1) to mice

and monkeys, using relevant doses for clinical use, no toxic effects were observed in specific target organs, including kidney, liver, central nervous system, or heart. Moreover, the mice did not show signs of toxicity due to free Mn-cations [116]. A systematic and comparative toxicity and safety animal study carried out by subcutaneous injection of Mn(III)T2EPyP$^{5+}$ and its analogs, Mn(III)T2BuOEPyP$^{5+}$ and Mn(III)T2HexPyP$^{5+}$, showed differences related to their different lipophilicities [21]. Mn(III)T2EPyP$^{5+}$ is the least toxic of these cationic Mn(III) porphyrins, mainly due to its very low ability to cross the BBB. This Mn(III)porphyrin gave a negative Ames test and a no-observed-adverse effect level (NOAEL) with 18 daily i.v. bolus injections, followed by 17 days of recovery. Cynomolgus monkeys were less sensitive to this drug than mice, with a histopathological-based NOEL of 15 mg kg$^{-1}$ *per* day. Concerning Mn(III)T2BuOEPyP$^{5+}$, no genotoxic risk was observed in humans, only a marginally positive Ames test and a NOAEL in mice of 12 mg kg$^{-1}$ *per* loading dose after 5-week daily injections, and a NOAEL in cynomolgus monkeys of 6 mg kg$^{-1}$ *per* dose loading for five consecutive weeks, followed by a 2-week recovery period. The highest toxicity was observed for the most apolar and lipophilic of the three investigated cationic complexes, Mn(III)T2HexPyP$^{5+}$. Due to its relatively high lipophilicity, this Mn(III) porphyrin distributes in all organs and therefore, it has dose-dependent toxicity. The $TD_{50}$ (the dose at which toxic effects were observed with 50% of the mice) of Mn(III)T2HexPyP is 12.5 mg kg$^{-1}$ (= 0.01 mmol kg$^{-1}$) when injected subcutaneously compared to 91.1 mg kg$^{-1}$ for Mn(III)T2EPyP (0.09 mmol kg$^{-1}$). The adverse effects observed were shaking and hypotonia. These toxic effects were reverted with no observable pathological changes during four weeks after the administration [21]. However, it should be taken into account that these toxicity studies were carried out at therapeutic concentration ranges that are about one order of magnitude lower than the typical necessary concentrations of Mn(III)porphyrins used as MRI CAs. Although the reported $TD_{50}$ values seem to indicate that MnT2EPyP$^{5+}$ is the most promising for MRI applications, *in vivo* MRI evaluation has yet to be carried out.

In conclusion, the studies described show that the lipophilicity, polarity, charge, size, shape, and bulkiness of the substituents at the parent porphyrin system determine their biodistribution and PK. An accurate and perfect balance of these chemical properties is required to fulfill the requisites for clinical use. An important factor is their *in vivo* toxicity, which is a consequence of their biodistribution and PK properties. The more lipophilic structures are distributed in all organs, including the brain, and preferentially in the liver, and have higher retention, slower liver excretion, which may cause higher toxicity. The more hydrophilic structures have more limited biodistribution and faster preferential renal excretion. However, these correlations are not at all linear and, besides lipophilicity and hydrophilicity, other factors like charge, size, and acid/base characteristics also influence the overall behavior of the Mn(III)-complexes, often in an unexpected way.

**5. Cell tracking**

Several meso-substituted porphyrins have been developed for application as cell tracking agents, particularly to visualize the initial steps in cell therapies including delivery, migration, and engraftment. Traditionally, superparamagnetic iron oxide nanoparticles (SPIONs) are used for the monitoring of cells. However, these CAs have the disadvantage that they are negative CAs: they produce a decrease in intensity, which is often more difficult to observe than the effect of positive CAs, like the Mn(III) porphyrins. The lipophilic tetraacetoxyethyl ester of Mn(III)TCP is a $T_1$ CA that easily crosses the cell membranes. Inside the cells, the ester is enzymatically cleaved by esterases in the cytosol to afford the corresponding carboxylate, Mn(III)TCP [50,117]. The latter does not leak out of the cell because it is more hydrophilic and negatively charged. Furthermore, outside of the cell, the ester is self-aggregated and consequently has a low relaxivity, whereas after hydrolysis inside the cell the aggregates break down to give rise to an increase in relaxivity (see Fig. 9). The sensitivity in mouse stem cells is 4 times as large as that of GdDTPA [117]. Moreover, the viability and the proliferation of the cells were not affected. Therefore, this CA is promising for stem cell tracking [117]. Similar agents (tetraacetoxyethyl ester of Mn(III)TCP and the tetraethyl ester of Mn(III)TCP) have been reported with improved performance and easier preparation procedures [118]. The tetraethyl ester of Mn(III)TCP has been shown to effectively label human embryonic stem cells at a very low concentration (10-40 μM) without affecting the viability. The agent localizes predominantly at the cell membrane and not in the nucleus [118]. Mn(III)TPPS$_3$A (structure, see Fig. 1) passed the cell membrane and even entered the nucleus [119]. It should be noted that the relaxivity of cell tracking CAs generally is lost after some time due to dilution when the cells concerned divide rapidly.

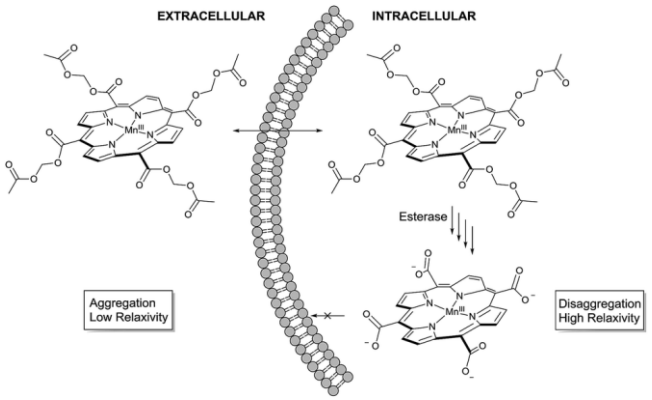


**Fig. 9.** Proposed mechanism for cell labeling with an ester of Mn(III)TPPC$_4$. Copied from ref. [50]. Published by The Royal Society of Chemistry.

**6. Responsive probes**

Abnormal redox potential and partial oxygen pressure ($pO_2$) are important diagnostic parameters for several diseases including cancer, inflammation, and cerebral infarcts. Therefore, there is a need for effective redox-responsive CAs. Since Mn can switch easily between the two- and three-valent oxidation states with different relaxation characteristics, Mn-based compounds may be interesting candidates for this class of CAs. Ideally, redox-responsive CAs should have the following properties [120]: (*i*) a redox half-cell potential that is accessible to biologically relevant reducing agents like glutathione (GSH); (*ii*) a ligand that stabilizes both Mn(II) and Mn(III) such that reduction or oxidation does not result in decomposition; (*iii*) turn-on of the imaging signal change upon activation; and (*iv*) kinetics that is rapid on the imaging time scale.

Aime et al. have exploited the difference in sensitivity of $r_1$ to $\tau_R$ between Mn(II) and Mn(III) for the design of a $pO_2$ sensitive CA [37]. Mn(III)$TPPS_4$ was reduced to Mn(II)$TPPS_4$ by dithionite, which was then used to cross-link poly-β-cyclodextrin (containing 3-9 monomeric CD units) through host-guest interactions between CDs and the phenyl sulfonate groups of $MnTPPS_4$. The interaction strengths of Mn(II) and Mn(III) with poly-β-CD are similar and the Mn(II) oxidizes easily in response to $pO_2$. The $r_1$ values in the Mn(II) and Mn(III) adducts are 40.8 and 15.2 $s^{-1}$ $mM^{-1}$ at 0.47 T and 298 K, respectively.

Pinto et al. have designed a modified probe in which the four phenyl sulfonate groups were replaced by 2,3,5,6-pentafluoro-4-(mPEG)phenyl groups. By the electro-withdrawing effect of the fluoro atoms, the stabilization of Mn(III) relative to the Mn(II) state was reduced. Consequently, these complexes can be reversibly and rapidly switched between these valence states by reduction with ascorbic acid or β-mercaptoethanol and oxidation with air. This probe exhibited a 3-fold increase in $r_1$ at 0.5 T and 298 K. At 1.5 T upon reduction, the increase was half as large. Unfortunately, reduction by glutathione or cysteine is prevented by the coordination of a carboxylate group of these compounds to Mn(III) at the axial position, as was evidenced by NMR data [51].

A $Zn^{2+}$-responsive CA has been constructed by replacing one of the phenyl sulfonate functions in Mn(III)$TPPS_4$ with a dipicoline derivative Mn(III)(DPA-C2)-$TPPS_3$ (Fig. 10) [121]. The idea is that two pyridine nitrogen atoms of this unit are coordinated to the axial sites of Mn(III) in the absence of $Zn^{2+}$ and thus blocks these sites for water coordination ($q$ = 0). After binding of $Zn^{2+}$, the DPA-C2 arms move away from the porphyrin to render Mn(III) available for two water molecules and this would rise $q$ to ultimately 2, which will be reflected in an increase in $r_1$. This appears to happen in solution but in cell culture, binding of $Zn^{2+}$ leads to an unexplained decrease in $r_1$, although $r_2$ increases. Since the binding of $Zn^{2+}$ also results in increased fluorescence, this compound can be applied as a dual MRI-fluorescence probe. Mn(III)(DPA-C2)-$TPPS_3$ penetrates cells more effectively

than the more polar Mn(III)TPPS$_4$ and is more persistent. This was demonstrated with intracranial injection in rats [122]. It provided relatively high contrast, particularly in the $Zn^{2+}$-rich hippocampus.

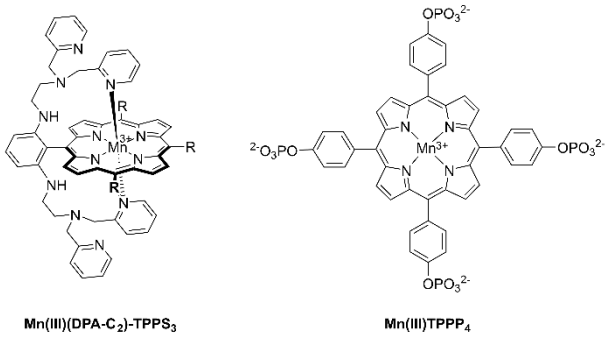


**Fig. 10.** Schematic representation of the molecular structures of the $Zn^{2+}$-sensor Mn(III)(DPA-$C_2$)-TPPS$_3$ (R = $SO_3^-$) and the gene expression detector Mn(III)TPPP$_4$.

A method has been proposed to detect gene expression *via* the secreted reporter enzyme alkaline phosphatase. In its presence, the phosphonate groups of Mn(III)TPPP$_4$ (see Fig. 10) were cleaved off resulting in the corresponding phenolic compound, which precipitated. As a result, the relaxivity dropped substantially as was demonstrated in both cell and *in vivo* studies [123].

A series of arachidonic acid-responsive CAs has been generated by directed evolution of the heme domain of Bacillus megaterium cytochrome P450 BM3 in the presence of Mn(III)PP [82]. The compound with the optimum response showed an $r_1$ decrease from 3.3 to 1.2 $s^{-1}$ $mM^{-1}$ upon addition of arachidonic acid, probably due to blocking of the water accessibility of Mn(III) by arachidonic acid.

Thermosensitive Mn(III)-based microgels have been prepared by cross-linking an Mn(III)-tetra(3-vinyl phenyl) porphyrin core with poly(alkyl acrylamides) [60]. Optimum results were obtained with N-isopropyl acrylamide, which gave a 3-dimensional network that decreases in hydrodynamic diameter from 133 to 103 nm between 298 and 310 K, respectively. This was accompanied by a sharp increase in $r_1$ (8.4 $\rightarrow$ 14.5 $s^{-1}$ $mM^{-1}$ at 3 T) as a result of the reduced mobility of the Mn(III) porphyrin cores.

## 7. Applications of Mn(III) porphyrins in MRI guided theranostics

The high stability and relaxivity of Mn(III) porphyrins and their preferential uptake by tumors make them efficient MRI CAs for cancer imaging. They also have optical and biological properties with potential therapeutic applications. These properties of Mn(III) porphyrins potentiate the

integration of the advantages of MRI as an imaging tool with different types of therapeutic approaches in MRI-guided theranostics. Here, some recent examples of such studies are described.

*7.1. MRI-guided chemotherapy*

Chemotherapy (CT) consists of the use of a chemical to treat a disease, usually applied to cancer, where a powerful drug kills fast-growing cancer cells in the body. It uses a large variety of biological mechanisms, including immunotherapy and gene therapy. However, most chemotherapeutic agents have their efficacy limited *in vivo* by short half-lives and undesirable side-effects due to toxicity to healthy tissues. To minimize these issues, nanocarriers have been developed which are able to selectively deliver the drug at the therapeutic site through controlled drug release, providing at the same time temporal control and protection of the therapeutic cargo. Some nanoplatforms have integrated Mn(III) porphyrins as MRI CAs with targeted drug delivery capabilities to improve their cancer therapeutic efficacy through MRI-guided drug delivery.

Mn(III)-labeled nanobialys have been developed as potential MRI theranostic NPs targeted to fibrin clots. These toroidal-shaped, 180-200 nm sized NPs were prepared by molecular self-assembly of amphiphilic branched polyethylenimine (PEI), forming inverted micelles, and including, at their surface, Mn(III)PP chloride as MRI contrast agent and biotin-caproyl-DSPE (Fig. 11) [100]. Their relaxivities at 1.5 T and 298 K were $r_1$ = 3.7 $s^{-1}$ $mM^{-1}$ Mn and $r_2$ = 5.2 $s^{-1}$ $mM^{-1}$ Mn, providing high particulate relaxivities. Nanobialys with biotin and Mn(III), with biotin and no Mn(III), and no biotin with Mn(III) were targeted *in vitro* to fibrin clots using avidin-biotin interactions and biotinylated fibrin-specific monoclonal antibodies. MRI images (3 T) of the clots only showed positive contrast enhancement of the fibrin-targeted Mn(III) nanobialys. Nanobialys loaded with both hydrophilic (DOX) and hydrophobic (camptothecin) chemotherapeutic agents released the drugs *in vitro*, demonstrating their potential utility for theranostic applications for microthrombi in ruptured atherosclerotic plaques [100].

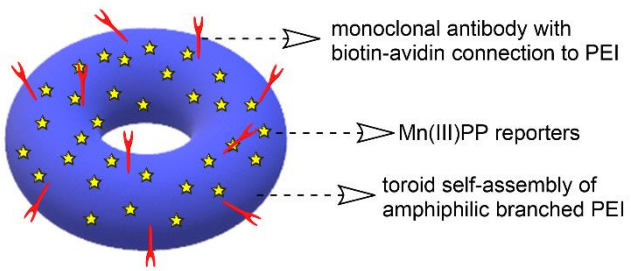

**Fig. 11.** Schematic representation of the structure of a bialys soft NP [100].

The controlled release of the therapeutic agent to increase its accumulation at the tumor target and drastically decreasing side effects can be performed by a variety of triggering signals, such as local pH changes. In order to also avoid the premature release of the MRI probe, theranostic NPs were prepared by covalent conjugation of Mn(III)$TPP_3A$ at the surface of DOX-loaded poly(lactic acid) (PLA) nanoparticles (MnP-DOX NPs) of 98.6 nm size for potential $T_1$-weighted MRI imaging and pH-sensitive drug delivery. The *in vitro* release of DOX from MnP-DOX NPs increased significantly under acidic conditions, while the MnP-DOX NPs were quickly internalized by HeLa cells and effectively suppressed their growth due to the accelerated drug release in acidic cell lysosomes. The MnP-DOX NPs had a much higher $r_1$ (27.8 $s^{-1}$ $mM^{-1}$ Mn) than Mn(III)$TPPS_3A$ (6.70 $mM^{-1}$ $s^{-1}$ Mn) at 0.5 T. Upon i.v. injection of these NPs in male nude mice bearing an HT-29 tumor, the tumor showed a selective positive contrast in $T_1$-weighted *in vivo* MRI images (7.0 T). Therefore, this nanoplatform was considered a promising tool for cancer MRI-guided responsive theranostics [66].

*7.2. MRI-guided hyperthermal therapy*

In hyperthermal therapy (HTT) a body tissue is exposed to higher than normal temperatures for the treatment of cancer. It uses several kinds of heating sources, such as light ranging from radio frequencies to microwaves, ultrasound waves, and magnetic fields (magnetic hyperthermia), which can induce moderate heating in a specific target region (local hyperthermia). Hyperthermia is defined as heating a tissue to a temperature in the range 314–320 K for a time period of tens of minutes. Thermal ablation involves the destruction of a tissue by extremely high (hyperthermia) or low (hypothermia) temperatures. In general, temperatures of either below 233 K or above 333 K cause complete cell necrosis almost instantaneously.

Photothermal therapy (PTT) is a form of HTT in which cancer tissues are destroyed by a controlled heat generation. This occurs through the interaction of electromagnetic radiation in the form of laser light (mostly in the NIR, which is more efficient in penetrating tissue and is less energetic, and therefore less harmful to surrounding cells and tissues) with photothermal agents, which mediate the conversion of light into heat. These agents, like photosensitizers, are activated by light with a specific frequency to an excited state, where it releases vibrational energy (heat) which kills the targeted cells. Unlike photodynamic therapy (PDT, see later), PTT does not require oxygen to interact with the target cells or tissues. Heating is localized to the tissue areas in which the applied light excites the photothermal agent that is distributed there. This provides excellent spatial control of the therapeutic process, minimizing off-target tissue damage. PTT is emerging as a minimally

invasive and highly effective therapeutical modality. Currently used photothermal agents include Au nanoshells and nanorods, as well as nanoscale graphene and graphene oxide sheets, which are efficient and photostable but not biodegradable [124].

Several studies were reported on the application of NPs that include Mn(III) porphyrins for MRI-guided PPT. One of these systems consists of PLA NPs entrapping DOX, which are surrounded by an Au nanoshell having a Mn(III) porphyrin derivative covalently linked to its surface through a PEG spacer (DOX@PLA@Au-PEG-MnP NPs) (Fig. 12). These NPs, with a diameter of 123.6 nm, showed excellent colloidal stability and long blood circulation time due to the presence of PEG. Under NIR light irradiation, the NPs showed an efficient photohyperthermic effect and a light-triggered release of DOX due to the high NIR light absorption coefficient of the Au nanoshell. The Mn(III) porphyrin (MnP) at the NPs surface provided a relaxivity ($r_1$ = 22.18 $mM^{-}1\ s^{-1}$ at 0.5 T and 310 K) three times higher than the free MnP. An *in vivo* MRI evaluation in HT-29 tumor-bearing nude mice showed a positive MRI contrast effect in the tumor region in $T_1$-weighted images, which could be used to accurately locate the tumor site to guide external NIR laser irradiation for photothermal ablation of the tumor. These *in vivo* experiments showed that the combination of CT and PTT based on the theranostic NPs provided a synergistically improved therapeutic effect compared with either therapy used separately [69].

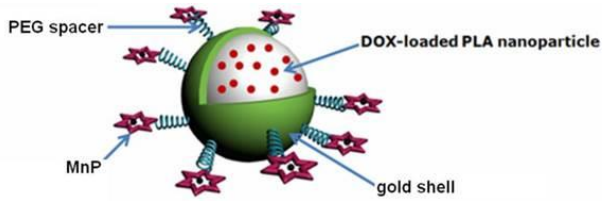


**Fig. 12.** Schematic representation of DOX@PLA@Au-PEG-MnP NPs. Copied from ref. [69].

An alternative is the use of porphysomes (PS), which are nanovesicles formed from self-assembled biocompatible porphyrin bilayers, with favorable optical, photothermal, and photoacoustic properties. Their large aqueous core can be loaded for multimodal theranostic applications [125]. Incorporation of $Mn^{3+}$ ions directly into the porphyrin building blocks of porphysome NPs led to Mn(III)-porphysome nanovesicles (MnPS), which were shown to be a non-toxic alternative to inorganic NPs for MRI-guided PTT (Fig. 13). The 120–130 nm size MnPS NPs incorporating 80000 porphyrins *per* particle, showed relaxivities $r_1$ = 1.2 $s^{-1}\ mM^{-1}$ and $r_2$ = 7.0 $s^{-1}\ mM^{-1}$ at 7 T, corresponding to *per* particle relaxivities of $r_1$ = 96000 $s^{-1}\ mM^{-1}$ and $r_2$ = 560000 $s^{-1}\ mM^{-1}$. The

MnPS originated positive contrast in $T_1$-weighted MRI phantom images. In addition to providing MRI contrast, the incorporation of paramagnetic $Mn^{3+}$ into the porphyrins has quenched their luminescence by promoting energy loss from their excited states via non-radiation decay pathways. Moreover, that suppressed their ability to generate reactive oxygen species (ROS) associated with PDT activity and self-destructive photochemical reactions, improving their photostability. Thus, the MnPS decay was purely in the photothermal mode, with high photothermal efficiency. These favorable properties are unprecedented for an organic NP system with a single functional component [86].

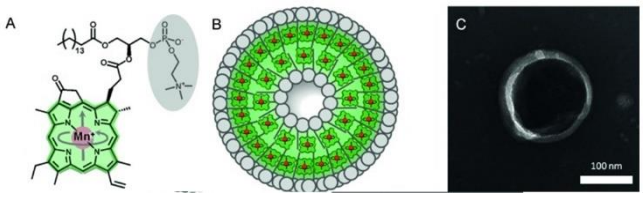


**Fig. 13.** A) Molecular structure of amphiphilic porphysome building block. B) Schematic representation of Mn-porphysome nanovesicles (not to scale). C) Representative TEM of Mn-porphysome NPs. Reproduced with permission from ref. [86] Copyright 2014 Wiley-VCH Verlag GmbH & Co. KGaA, Weinheim.

Another organic nano-micelle platform was developed based on the amphiphilic poly[(poly(ethylene glycol) methyl ether methacrylate)-co-(3-aminopropyl methacrylate)]-block-poly(methyl methacrylate) (P(PEGMA-co-APMA)-b-PMMA) block copolymer prepared using the reversible addition-fragmentation chain transfer radical polymerization technique. Multifunctional micelles were developed by self-assembly of the copolymer molecules, crosslinking of the shell with the photosensitizer $TPPC_4$ as a photodynamic agent, and fluorescence indicator, which was labeled with Mn(II) ions (which oxidize spontaneously to Mn(III)) to act as an MRI contrast agent. Non-covalent incorporation of the IR825 dye in the micelle core provided photoacoustic (PA) imaging ability and a photothermal effect (IR825@P(PEGMA-co-APMA)-b-PMMA@$TPPC_4$/Mn NPs) (Fig. 14). These biocompatible NPs of 80 nm size were highly soluble and stable in a physiological medium. They also had high singlet oxygen ($^1O_2$) generation yield upon irradiation at 660 nm and high photothermal conversion efficiency during exposure to 808 nm laser light. The *in vitro* relaxivity of the NPs was $r_1$ = 9.53 $s^{-1}$ $mM^{-1}$ at 3.0 T. Their use as a theranostic agent for the combined effect of PTT and PDT cancer treatment was evaluated *in vitro* in 4T1 cells. They had high *in vivo* tumor uptake with a long blood circulation half-life (~3.64 h) by the EPR effect after i.v. injection in 4T1 tumor-bearing Balb/c mouse model, as shown by fluorescence, a positive contrast of the tumor in $T_1$-

weighted MRI images and PA imaging. *In vivo* anti-tumor effects were demonstrated by combined PTT and PDT with a much improved synergistic therapeutic effect in both superficial and deep regions of the tumor [64].

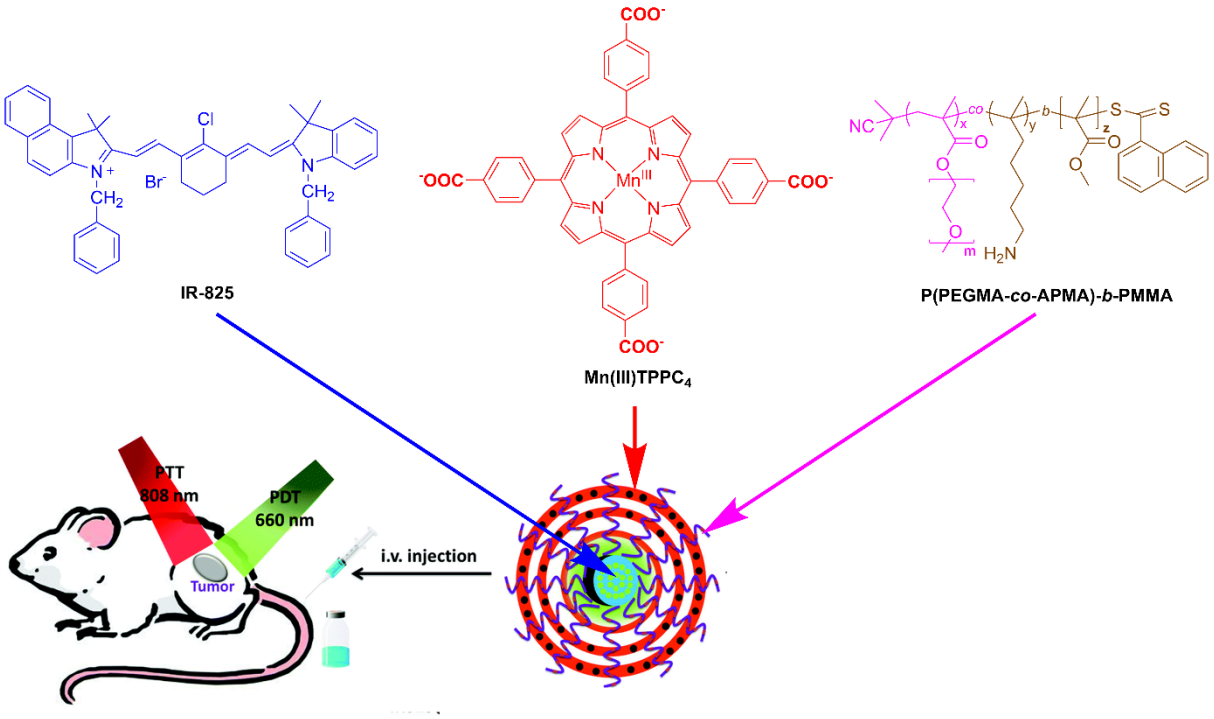


**Fig. 14.** Schematic illustration of the construction of multi-modality CA for MRI imaging-guided photothermal and photodynamic therapy. Adapted with permission from ref. [64] Copyright 2016 The Royal Society of Chemistry.

Several nanoscale metal-organic framework (NMOF) systems for MRI-guided PTT have recently been reported. An NMOF was prepared hydrothermally from biocompatible $Zr^{4+}$ ions, the Mn(III)-$TPPC_4$ porphyrin as a bridging ligand (Fig. 15), and *S*-nitrosothiol (SNO) conjugated to the surfaces of the NMOF (NMOF–SNO), for MRI-guided PTT and nitric oxide (NO) delivery. The NMOF–SNO particles were spindle-shaped of 60 × 140 nm size, with triangular channels 1.25 nm size. In water solutions, they had a hydrodynamic size of 265.5 nm, with a relaxivity $r_1$ = 26.9 $s^{-1}$ $mM^{-1}$ at 1.2 T and 298 K. The Mn(III)$TPPC_4$ porphyrin provided strong $T_1$-weighted MRI positive contrast, while SNO was used for heat-sensitive NO generation upon irradiation with NIR light, which also triggered the photothermal effect. Upon i.v. injection into MCF-7 tumor-bearing nude mice, NMOF–SNO readily accumulated in the tumor, as shown by its strong positive contrast in $T_1$-weighted MRI images (3 T) at 1 h post-injection. When exposed to a NIR laser, the growth of the tumors of mice injected with

NMOF–SNO was completely inhibited. Thus, the NMOFs–SNO is an effective theranostic system for MRI-guided NO release and PTT synergetic therapy upon a single NIR irradiation [102].

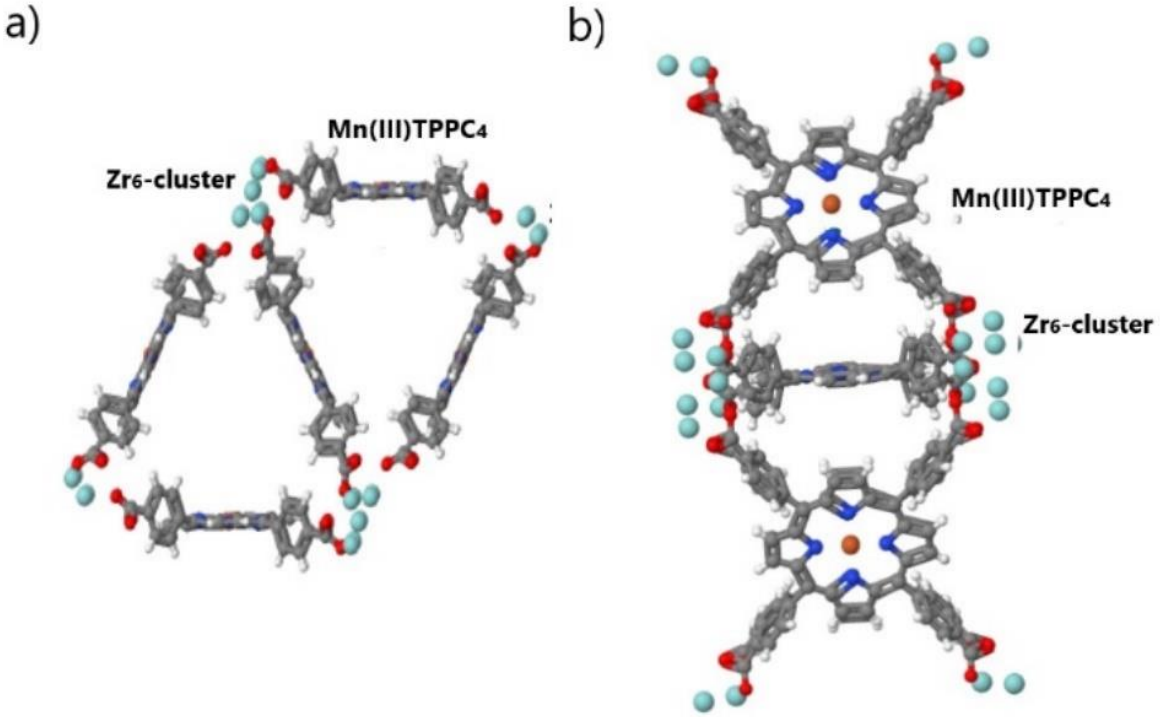


**Fig. 15.** The unit cell of PCN-23, a) viewed down the triangular channels, b) viewed perpendicular to the triangular channels. Retrieved from The Cambridge Crystallographic Data Centre, deposition number 1016164 [126]. In NMOF-SNO, the $TPPC_4$ ligands are loaded with Mn(III) and SNO is conjugated at the surfaces [102].

Another NMOF was also synthesized using a hydrothermal method from a $Hf_6$ cluster and $Mn(III)TCPP_4$, followed by functionalization with folic acid (FA) at the Hf nodes to give the multifunctional theranostic targeted nano agent FA-Hf-Mn-NMOF (Fig. 16). These NPs were characterized *in vitro*, showing spindle shapes with long and short average diameters of 93.4 nm and 32.3 nm, respectively, high photostability and high photothermal conversion efficiency upon 808 nm laser irradiation. While no cytotoxicity was observed on HeLa cells in the presence of the FA-Hf-Mn-NMOF without irradiation, their irradiation with an 808 nm laser for 10 min or with 4 Gy X-rays, separately or together, led to a dramatic and synergistic decrease of cell survival, showing their potential as activators for synergistic PTT/radiotherapy (RT) of tumors. Furthermore, FA-Hf-Mn-NMOF generates $O_2$ from $H_2O_2$ and $^1O_2$ upon X-ray irradiation. It has a high relaxivity, $r_1$ = 16.75 $s^{-1}$ $mM^{-1}$, at 3 T, and the NPs are efficiently internalized into HeLa cells, as shown by cell brightening in

$T_1$-weighted MRI after cell uptake. An *in vivo* study using BALB/c mice with subcutaneously implanted S180 tumor cells indicates that the agent has good biocompatibility, tumor targeting, positive contrast in $T_1$-weighted MRI, as well as CT attenuation due to the presence of the high-Z Hf atoms, and PAI contrast due to the photothermal properties of Mn(III)TCPP$_4$. It showed to be effective in imaging-guided synergistic PTT/RT of tumor [127].

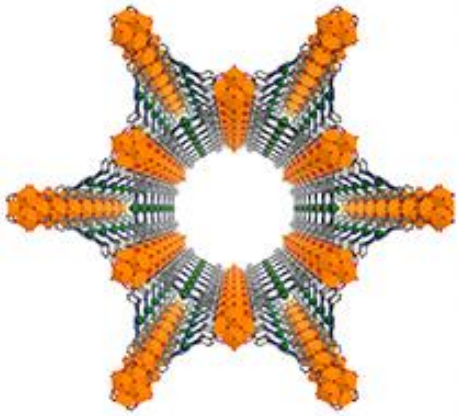

**Fig. 16.** Structure of Hf-Mn-NMOF viewed down the channel. The $Hf_6$-clusters (in orange) are connected through Mn(III)TPPC$_4$ complexes. In FA-Hf-Mn-NMOF, folic acid is coordinated to the Hf-clusters. This framework is the Hf-analog of the PCN-222 framework shown in Fig. 19. Image copied from ref. [127].

*7.3. MRI-guided radiation therapy*

Radiotherapy uses high-energy ionizing radiation, generally as part of cancer treatment, to control the growth or kill malignant cells. However, RT usually has side effects, inducing lesions on all irradiated tissues. RT damages the cell DNA, and when this cannot be repaired, they stop dividing or die. The ionizing radiation in RT can also produce high levels of reactive oxygen species (ROS), such as peroxides (ROOH), superoxide ($O_2^-$), singlet oxygen ($^1O_2$), and hydroxyl radicals (•OH), and reactive nitrogen species (RNS), like peroxynitrite. In a biological environment, this results in further DNA damage of the cells (oxidative stress). However, this strong radiosensitizing effect of oxygen, which strongly increases the effectiveness of a given radiation dose, can be limited by the tendency of the cells of solid tumors to become oxygen deficient when their growth is faster than their blood supply. A hypoxic environment makes tumor cells much more resistant to radiation damage than a normoxic one. One of the ways to overcome this problem is to use hypoxic cell radiosensitizers such as misonidazole and metronidazole.

Differential effects of Mn(III) porphyrins, consisting of anti- and pro-oxidative reactions, on normal versus cancer cells are controlled by their differential redox environments. Mn(III) porphyrins have been successfully used preclinically as adjuvants to radiotherapy of tumors of multiple histologies, including brain, breast, prostate, and melanoma [128]. An example is the effect of the SOD mimetic $[Mn(III)T2EPyP]^{5+}$ (Structure, see Fig. 1) on the radio responsiveness of rodent tumors. It was shown that $[Mn(III)T2EPyP]^{5+}$ increases radiation-induced damage to the tumor vasculature through its antiangiogenic effect as anti-oxidative scavenger of radiation-produced ROS/RNS that promotes vascular angiogenesis while protecting normal tissues from radiation injury through their pro-oxidant properties as scavengers of ROS/RNS [115].

MRI-guided radiation therapy is a promising approach for improving the clinical outcomes of patients treated with RT [129]. Mn(III)-porphyrins have been used as RT sensitizers [21,115,128] and as tumor-specific MRI contrast agents. MRI-guided RT studies using Mn(III) porphyrins as CAs and selective RT sensitizers have been suggested [130] and reported in the literature [131]. In this study, a conjugate of Mn(III)KADTF (an Mn(III)PP derivative with the hypoxic radiosensitizer 2-nitroimidazole KU2280 at a side chain, see Fig. 2) was initially tested *in vitro* with HeLa cells, showing enhancement of the effect of radiation under hypoxic conditions. Injection of the Mn(III) KADTF conjugate (0.1 mmol $kg^{-1}$) into the tail vein of SCCVII tumor-bearing C3H/HE mice, led to positive contrast-enhanced $T_1$-weighted images (at 1.5 T) of the tumor after 1.5 h. MRI-guided RT at 20 Gy 1.5 h after infusion of KADTF (0.15 mmol $kg^{-1}$), inhibited tumor growth more significantly than a single radiation treatment at the same dose. These results indicate that the Mn(III) porphyrin promoted the transfer of the 2-nitroimidazole to the tumor. No toxicity effects were observed, with an $LD_{50}$ > 0.8 mmol $kg^{-1}$. The results of this study show that effective MRI-guided RT of tumors is possible [131].

*7.4. MRI-guided photodynamic therapy*

Besides ionizing radiation, the ROS/RNS can be produced by environmental stress triggered by light, heat, and sound. Photodynamic therapy (PDT) is based on the cell destruction caused by toxic singlet oxygen ($^1O_2$) and/or other ROS produced within the cells by the effect of light through a sequence of photochemical and photobiological processes. These processes are initiated by the reaction of a photosensitizer (PS) with tissue oxygen upon light irradiation with a specific wavelength in the visible or NIR region. The decay of the excited singlet state of the PS should mainly occur through intersystem crossing to efficiently populate an excited triplet state ($^3PS^*$). The latter can produce toxic ROS, such as $^1O_2$, by first reacting with other molecules, generating intermediate free radicals that yield ROS (type I photochemistry). However, the most relevant mechanism is a direct energy transfer from $^3PS^*$ to molecular oxygen in its ground triplet state ($^3O_2$) producing cytotoxic $^1O_2$ (type

II photochemistry), because most PSs are very effective in producing $^1O_2$. The ROS produced inside the cells cause irreversible damage, in particular to mitochondria, triggering cell apoptosis, if PSs can accumulate there. PDT can selectively kill cancer cells if PSs can accumulate in them. An ideal PS should follow several requirements: a) have high selectivity for cancer cells; b) be able to produce ROS efficiently; c) show efficient NIR (700-800 nm) light absorption; d) have no dark toxicity and minimal skin photosensitivity; e) be amphiphilic for optimal absorption, distribution, metabolism, and excretion; f) be stable and easy to dissolve in injectable solvents; g) be chemically pure and easy to prepare.

PDT has been clinically approved in the treatment of dermatological and ocular disorders, as well as of various early-stage superficial tumors. Its main advantages are that it is a localized treatment, with minimal invasiveness and side effects, while a main disadvantage is low tissue penetration depth due to light scattering and absorption by endogenous molecules. Several classes of PSs have been studied, such as porphyrin-type compounds, phthalocyanines, naphthalocyanines, and their metallated analogs such as Al, Co, Si, Zn, and Lu complexes or expanded porphyrins related to texaphyrin [132]. Several PSs are at various stages of advanced clinical and preclinical studies, such as Photofrin®, Levulan®, Radachlorin®, Visudyne®, Foscan®, and Tookad® [133]. Porphyrin and phthalocyanine conjugates with $Gd^{3+}$ complexes have been developed as PSs for MRI-guided PDT [134], while the corresponding theranostic agents based on NPs have also recently been reviewed [135–137].

Several nanoplatforms incorporating Mn(III) porphyrins have been reported for MRI-guided PPT, including the one reported in section 7.2 above for combined PTT/PDT [64]. The encapsulation of hydrophobic PSs within liposomes prevents their aggregation in aqueous media, which causes self-quenching, and improves their target delivery and ROS production. Many types of nanocarriers, such as polymeric micelles, conjugated polymer NPs, and silica NPs, have been used to obtain stable aqueous PS dispersions. However, they often have poor drug loading or increased self-aggregation of the entrapped PS, leading to self-quenching and almost no photosensitizing effect [138]. This is what happens to porphysomes, despite their high absorption in the NIR.

Liang *et al*. developed a theranostic nanocarrier for MRI-guided PDT cancer therapy with a high PS loading that did not leach out. This agent consisted of porphyrin dyad NPs (TPD NPs, see Fig. 17), containing two types of porphyrins: Mn(III)$TPPS_3A$ located in a hydrophilic shell as an MRI CA, and the metal-free porphyrin $TPPS_3A$ in a hydrophobic core functioning as a photosensitizer for PDT. The free $TPPS_3A$ was covalently grafted to a lipid (PGL) [70]. The PDT and MRI properties of the TPD NPs were optimized at a porphyrin/Mn(III) porphyrin ratio of 40.1%. The TDP NPs were spherical with

~60 nm size and the quenching of the production of $^1O_2$ by the PGL porphyrin due to the Mn(III) porphyrin present at the surface was minimized. Their relaxivity, $r_1$ = 20.58 $s^{-1}$ $mM^{-1}$ at 0.5 T and 298 K, was four times higher than for free Mn(III)TPPS$_3$A (5.16 $s^{-1}$ $mM^{-1}$) due to the immobilization on the NPs. The NPs were passively taken up by HeLa tumor cells. After 24 h i.v injection of the optimized TPD NPs to nude mice bearing the HT-29 tumor, $T_1$-weighted MRI images (at 7.0 T) showed a positive contrast of the whole tumor area relative to the surrounding healthy tissue (Fig. 18), allowing to guide laser light to the desired tumor site for PDT ablation, which was 100 % within 7 days in the presence of TPD NPs [70].

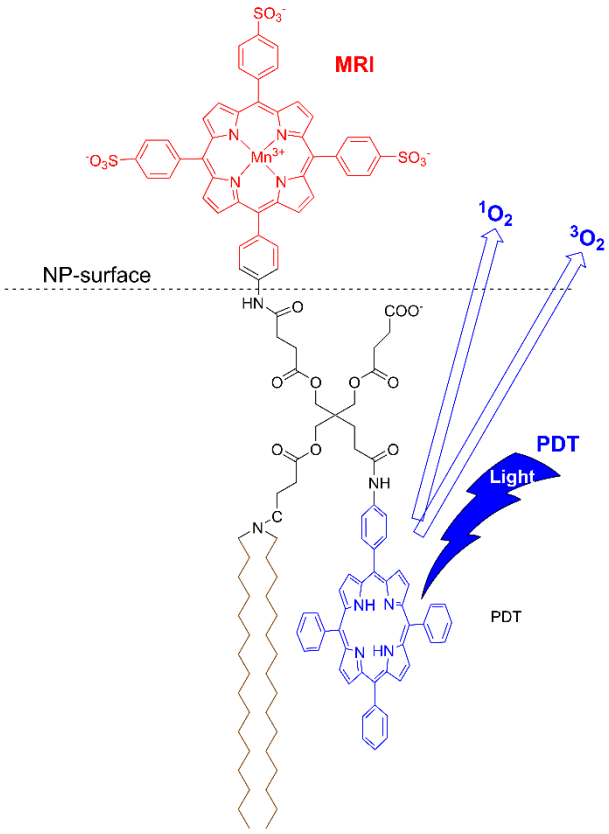


**Fig. 17.** Schematic representation of porphyrin dyad nanoparticles for MRI-guided PDT [70].

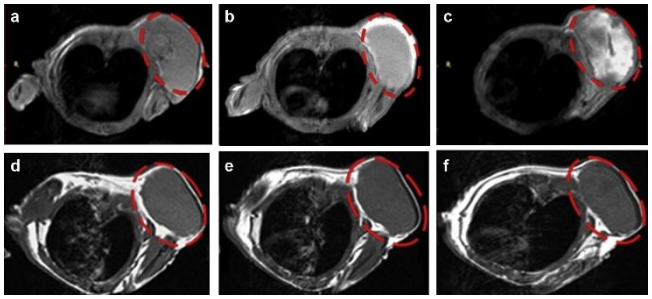

**Fig.18.** *In vivo* $T_1$-weighted MRI images of nude mice bearing HT-29 tumor before and after administration of TPD NPs with the Mn-porphyrin/PGL molar ratio of 40.1 % (a-c) and PGL NPs (d-f) acquired at different time intervals: before (a, d) and after injection for 30 min (b, e) and 24 h (c, f). Copied with permission from ref. [70] 2014 copyright Elsevier Ltd.

To overcome the severe limitations of the therapeutic effect of PDT in hypoxic tumor regions, due to the essential role of molecular oxygen in this modality, a porous NMOF NP was developed for MRI-guided PDT with the capacity of generation $O_2$ from $H_2O_2$ present in hypoxic tumors. This system (PCN-222(Mn)) was prepared from a hydrothermal reaction of Mn(III)TPPC$_4$ with $Zr^{4+}$ ions as $Zr_6$ clusters (Fig. 19). PCN-222(Mn) NPs had an olive-like shape with 300 × 130 nm sizes, that were stable in aqueous solution and had a high relaxivity $r_1$ = 35.3 $s^{-1}$ $mM^{-1}$ (1.0 T) due to the uniform distribution of $Mn^{3+}$ ions in the open framework (pore size: 3.7 nm) and to the high water affinity of the channels. It also showed good catalase-like catalytic conversion of $H_2O_2$ into $O_2$ by the Mn(III)TPPC$_4$, with potential for improving tumor hypoxia during PDT. An i.v. injection of PCN-222(Mn) into 4T1 tumor-bearing mice induced a long-lasting and high positive contrast of the tumor in $T_1$-weighted MRI *in vivo* images. It also effectively inhibited the tumor growth upon single-laser irradiation, reflecting the effective local generation of $^1O_2$ and MRI-guided PDT effect [65].

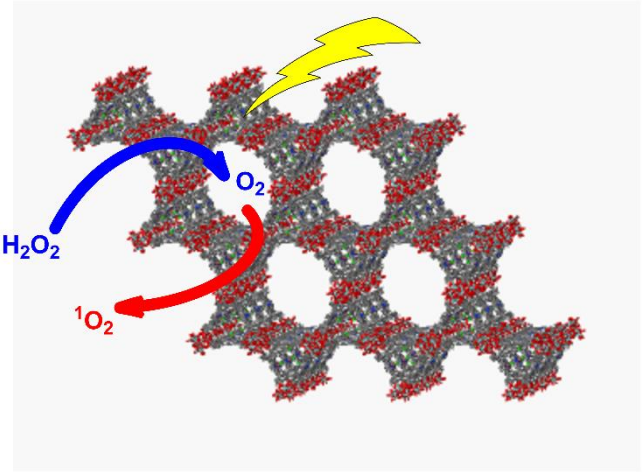


**Fig. 19.** The catalytic decomposition of $H_2O_2$ into $O_2$ and the formation of $^1O_2$ by light in NMOF PCN-222. In the framework, the vertices are occupied by $Zr_6$-clusters (red) and the edges by Mn(III)TPPC$_4$ molecules (gray) Ref. [65]. The framework is retrieved from The Cambridge Crystallographic Data Centre, deposition number 893545 [139].

Finally, a new porphyrin-based photosensitizer (Pt-Mn(III)Por-PPh$_3$) was prepared for integrated MRI and fluorescence imaging and mitochondrial-targeted PDT. The lipophilic

triphenylphosphonium cation, used as a mitochondria-targeted agent, was conjugated with the Mn(III)-hydroxy tripyridylphenoxyporphyrin (MnPor) through an alkyl chain, and subsequently coordinated at the pyridine rings with trans-platin to yield (Pt-Mn(III)Por-$PPh_3$) (Fig. 20). Under laser light irradiation for 10 min, HeLa cells treated with 50 μg $mL^{-1}$ of the Pt-Mn(III)Por-$PPh_3$ had reduced viability with an $IC_{50}$ of 30.74 μg $mL^{-1}$, which was attributed to the high ROS production and PTT effect of Pt-Mn(III)Por-$PPh_3$. Its fluorescence properties were exploited to study the cellular uptake and subcellular localization by confocal laser scanning microscopy, showing good mitochondrial-targeting in HeLa cells. Due to the Mn(III) porphyrin unit, the Pt-Mn(III)Por-$PPh_3$ gave good positive contrast in $T_1$-weighted MRI images (at 3 T) of phantoms [140].

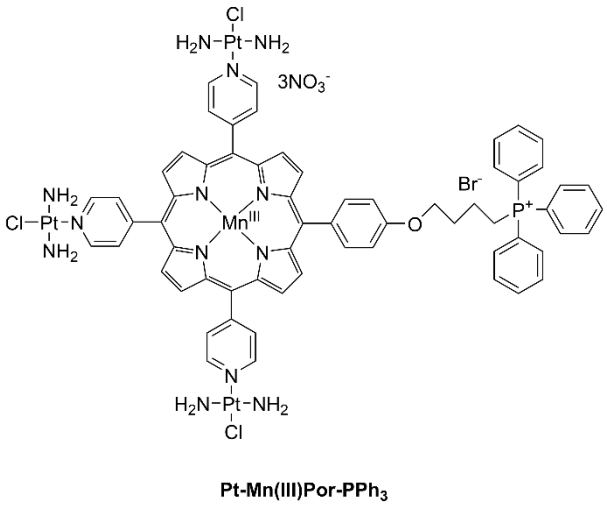


**Pt-Mn(III)Por-$PPh_3$**

**Fig. 20**. Molecular structure of Pt-Mn(III)Por-$PPh_3$

*7.5. MRI-guided sonodynamic therapy*

Sonodynamic therapy (SDT) is an anticancer therapy involving a chemical sonosensitizer (a drug that only becomes cytotoxic upon exposure to ultrasound) and high-intensity focused ultrasound. This technique is non-invasive, accurate, efficacious, and safe because the drug dose and the US irradiation power used can be reduced. In SDT, the cytotoxicity is originated from the ROS produced, triggered by ultrasonic stimuli. The process consists of several phases: a) the therapeutic US transducer (0.5 - 3.0 MHz frequency), consisting of a piezoelectric material to which an alternating voltage is applied, emits a focused beam, which creates high pressure inside the tumor area; b) this induces oscillating bubbles in the medium (cavitation); c) bubbles collapse under high pressure and induce various stresses – a shock wave, formation of •OH and •H radicals, and high temperatures; d)

the collapsing bubbles lead to the creation of ROS derived from the sonosensitizer; e) the ROS kill the cancer cells through the induced oxidative stress. The potential for cellular damage and range of action of the created ROS depend mainly on their half-life. In a biological environment, the generated ROS depend on the nature of the sensitizer. Several organic sonosensitizers have been reported in preclinical and clinical studies, such as 5-aminolevulinic acid, chlorins, porphyrin derivatives, and phthalocyanines, that accumulate preferentially in tumor zones. Inorganic $TiO_2$ nanoparticles have also been used, but biodegradation and biosafety issues have been the main obstacles to their clinical translation. An important advantage of SDT relative to PDT is that US energy can be targeted directly onto deep-seated cancer sites, as opposed to the low penetration of light through the skin and tissues, which limits PDT to the treatment of superficial and endoscopically reachable tumors [141].

Several Mn(III) porphyrin-based systems have been described for MRI-guided SDT. For example, the potential of poly(methyl methacrylate) (PMMA) core-shell NPs loaded with the $TPPS_4$ ($TPPS_4$-PMMA NPs) as a sonosensitizer associated with shockwaves (SWs), was investigated. These core-shell NPs were obtained by an emulsion polymerization reaction of methacryloyloxy-undecyl-dimethyl-ethyl ammonium bromide and methylmethacrylate and had an average hydrodynamic diameter of 93 nm. The positively charged ammonium groups located at the surface allowed loading the NPs with the negatively charged TPPS. The resulting $TPPS_4$-PMMA NPs were stable in physiological medium, with no release of $TPPS_4$. The cytotoxic effect of the sonodynamic treatment with the NPs and SWs was investigated on the human neuroblastoma cell line, SH-SY5Y. Cell proliferation decreased after SDT with the NPs and SWs, with an increase in necrotic (16.91%) and apoptotic (27.45%) cells at 48 hours. A 15-fold increase in ROS production compared to free $TPPS_4$ was achieved after 1 hour. Therefore, the sonosensitizing properties of $TPPS_4$ were significantly enhanced once loaded onto the NPs [142]. This study of the $TPPS_4$-PMMA NPs was exploited for the construction of *in vivo* sonosensitizing systems, PET radiotracers, and MRI CAs, by loading the positively charged PMMA NPs with $TPPS_4$ for SDT anticancer treatment, with $^{64}Cu(II)TPPS_4$ for biodistribution studies by PET imaging or with $Mn(III)TPPS_4$ for evaluation of their tumor accumulation by MRI. The $TPPS_4$-PMMA NPs showed favorable biodistribution in the tumor of a Mat B III syngeneic rat breast cancer model as shown by PET analysis. SW SDT responsiveness was confirmed by a 50 % decrease in tumor volume between pre- and post-treatment as measured in MRI images (Fig. 21). Treatment with $TPPS_4$-PMMA NPs plus SW appeared to be much more effective than with free $TPPS_4$ [143].

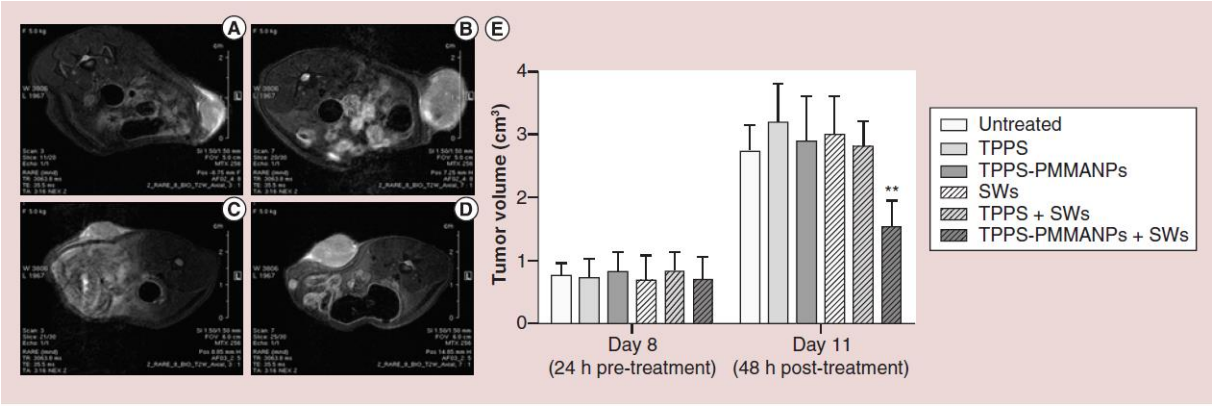


**Fig. 21.** Effect of SDT on Mat B III/Fisher 344 tumor growth. Rats with growing tumors were treated with TPPS, TPPS-PMMA NPs or SWs alone and in combination (10 mg/kg body weight intravenous and 0.88 mJ/cm$^2$ for 500 impulses, four impulses/s, respectively) on day 9 from tumor cells inoculation and tumor volumes were determined by MR at day 8 and 11. Representative $T_2$-weighted images of control (A, B) and TPPS-PMMANPs and SW-treated (C ,D) rats at day 8 (24 h pretreatment [A ,C]) and 11 (48 h post-treatment [B ,D]). The tumor volumes, at day 8 and day 11, of each experimental group, are reported as mean ± standard deviation for at least three separate experiments each in at least four animals per group (E). Copied with permission from ref. [143] 2015 Copyright Future Medicine Ltd.

Multifunctional surface PEGylated mesoporous organosilica nanoparticles with the organic sonosensitizer protoporphyrin (PP, see Fig. 2) and the paramagnetic Mn(III)PP MRI CA conjugated through amidation with 3-aminopropyl)triethoxysilane bound at their inner pore surfaces were developed for efficient *in vivo* MRI-guided SDT cancer theranostics. The spherical mesoporous structure of the NPs with 50 nm average size, allowed the $^1O_2$ generated upon US irradiation to freely diffuse out of the mesopores (3.4 nm size) to cause the SDT effect. This structure, with a large surface area, also maximized the accessibility of water molecules to the paramagnetic Mn(III) ions, leading to high MRI relaxivity ($r_1$ = 9.43 s$^{-1}$ mM$^{-1}$). The highly biocompatible NPs were efficiently endocytosed into 4T1 cancer cells and biodegraded by intracellular glutathione. They also showed high SDT efficiency for inducing cancer-cell death *in vitro*. I.v. administration of the NPs into 4T1 tumor-bearing BALB/c nude mice increased *in vivo* $T_1$-weighted positive contrast of the tumor and suppressed the tumor growth *in vivo* upon US irradiation [144].

To improve the efficacy of SDT in hypoxic tumor regions, a new carrier system was developed based on red blood cells (RBC) with high concentrations of catalase to decompose tumor endogenic $H_2O_2$ into $O_2$ and combine SDT and chemotherapy. RBCs were loaded with the hydrophilic Mn(III)TPPS$_4$ as sonosensitizer and MRI CA and the DOX drug to obtain DOX/Mn-TPPS$_4$@RBCs. The NPs had high catalase activity *in vitro* with efficient $O_2$ production, which promoted the rupture of the RBCs and showed improved release of DOX under US irradiation. Hemoglobin (Hb) was

simultaneously oxidized into highly oxidative ferryl-Hb species by $H_2O_2$ and ROS, resulting in cytotoxicity. Ferryl-Hb, with a longer half-life than the ROS, can diffuse further in cancer cells and cause more oxidative damage than the conventional ROS. The improved cytotoxicity of the RBCs/$H_2O_2$/US combination was verified in MCF-7 cells, which took up the NPs as shown by fluorescence microscopy. Aqueous solutions of the loaded RBCs had a high relaxivity, $r_1$ = 18.32 $s^{-1}mM^{-1}$ at 3 T, showing their potential to enhance the MRI signal intensity of a tumor site. The *in vivo* behavior of the NPs was studied in MCF-7 tumor-bearing mice after i.v. administration using $T_1$-weighted MRI and fluorescence imaging using the NPs labeled with the fluorescent dye IR783, showing that the new system overcame hypoxia in the tumor and improved the efficacy of SDT in this combination therapy [145].

*7.6. MRI-guided neutron capture therapy*

Neutron capture therapy (NCT) is another nonsurgical therapeutic modality for treating localized tumors. A patient is first injected with a tumor-localizing drug containing the non-radioactive isotope boron-10 ($^{10}B$) with a natural abundance of 20%, which has a much higher capacity (cross-section) to capture neutrons than other elements present in tissues. After neutron irradiation from a nuclear reactor or an accelerator, the neutrons lose energy when they penetrate the tissue and are selectively captured by the $^{10}B$ nuclei present preferentially in the tumor cells. The $^{10}B$ nuclei emit high-energy alpha particles in a $^{10}B$ (n, α)$^7Li$ nuclear reaction that kill adjacent cells. Although the use of other non-radioactive isotopes such as $^{157}Gd$ (natural abundance of 15.65%) has been studied, the only clinical experience is with $^{10}B$, known as boron neutron capture therapy (BNCT) [146,147].

The affinity of porphyrins for tumors has been exploited in studies of BNCT with porphyrins conjugated with boron cages and transition metal complexes of these compounds, including Mn [147]. The complex Mn(III)BOPP (see Fig. 2) has been suggested for application as theranostic in MRI-guided BNCT [91]. Its performance was compared with that of Mn(III)$TPPS_4$. The 0.25 T relaxivity of Mn(III)BOPP was 3.60 and 4.43 $s^{-1}$ $mM^{-1}$ at 298 K and 310 K, respectively. Upon i.v. injection, Mn(III)BOPP selectively localized in a rat 9L gliosarcoma, as shown by the observed positive contrast of the tumor *versus* the normal brain in $T_1$-weighted MRI images (1.5 T). A maximum contrast enhancement was observed 24 hours after injection, whereas maximum relaxivity was reached with Mn(III)$TPPS_4$ already after 5 min. Thus, Mn(III)-BOPP had a slower tumor uptake than Mn(III)$TPPS_4$ but longer retention in the tumor, making it potentially effective as an agent for BNCT.

Finally, the most relevant MRI-guided theranostic systems discussed in this section, which have been applied for in vivo tumor animal models, are summarized in Table 3.

**Table 3**. Examples of $Mn^{III}P$ MRI-guided theranostic systems with *in vivo* applications

| System | Techniques | $r_1$ ($B_o$) $mM^{-1}\ s^{-1}$ Mn (T) | Use/animal tumor model | Refs |
|---|---|---|---|---|
| DOX@PLA@MnP | MRI/chemotherapy | 27.8 (0.5) | $T_{1w}$ MRI (7 T) of acid pH triggered DOX release/HT-29 mice | 66 |
| DOX@PLA@Au-PEG@MnP | MRI/PTT | 22.2 (0.5) | $T_{1w}$ MRI of NIR triggered DOX release/HT-29 mice | 69 |
| IR825@P(PEGMA-co-APMA)-b-PMMA@MnTPPC$_4$ | MRI/PTT/PDT | 9.5 (3.0) | $T_{1w}$ MRI, PAI and fluorescence of NIR induced PTT/PDT by $TPPC_4$ sensitizer /4T1 Balb/c mice | 86 |
| $Zr_6$-SNO-MnTPPC$_4$ NMOF | MRI/PTT/chemotherapy | 26.9 (1.2) | $T_{1w}$ MRI (3 T) of NIR induced PTT by $TPPC_4$ sensitizer and chemotherapy by NO release/MCF-7 BALB/c mice | 102 |
| FA-$Hf_6$-MnTPPC$_4$ NMOF | MRI/PTT/RT | 16.7 (3.0) | $T_{1w}$ MRI (3 T) of NIR induced PTT by $TPPC_4$ sensitizer and RT by X-rays induced $^1O_2$ /S180 BALB/c mice | 127 |
| MnKADTF | MRI/RT | not reported | $T_{1w}$ MRI (1.5 T) of X-rays and KU2280 nitroimidazole induced RT/SCCVII C3H/HE mice | 130 |
| MnTPPS$_3$A-PGL-TPPS$_3$A polymer | MRI/PDT | 20.6 (0.5) | $T_{1w}$ MRI (7 T) of NIR triggered PDT by $TPPS_3A$ sensitizer/SCCVII C3H/HE mice | 70 |
| $Zr_6$-MnTPPC$_4$ NMOF (PCN-222(Mn)) | MRI/PDT | 35.3 (1.0) | $T_{1w}$ MRI of NIR induced PDT by $TPPC_4$ sensitizer and $O_2$ release of hypoxic tumor/4T1 Balb/c mice | 65 |
| MnTPPS$_4$-PMMA polymer | MRI/SDT | not reported | $T_{1w}$ MRI of US induced SDT by $TPPS_4$ sensitizer /Mat B III/Fisher 344 mice | 143 |
| HMONs-MnPpIX-PEG | MRI/SDT | 9.4 | $T_{1w}$ MRI of US induced SDT by PP sensitizer/4T1 Balb/c mice | 144 |
| DOX/Mn-TPPS$_4$ IR783@RBCs | MRI/SDT/chemotherapy | 18.3 (3.0) | $T_{1w}$ MRI of US induced SDT by $TPPS_4$ sensitizer and chemotherapy by ferryl-Hb/MCF-7 mice | 145 |
| MnBOPP | MRI/NCT | 3.6 (0.25) | $T_{1w}$ MRI (7 T) of BNCT /9L gliosarcoma rat | 91 |

## 8. Conclusions

During the last decades, great progress has been made in the development of Mn(III)-porphyrins as Gd-free alternatives for the classical Gd-based MRI CAs. Optimal relaxivity can be obtained for complexes in which the tendency for self-association can be suppressed. Particularly, Mn(III) complexes of the fully synthetic porphyrins with charged groups at the *meso*-positions are useful in this respect because for these complexes, generally, two water molecules are present in the first coordination sphere of Mn(III) and then $r_1$-values for low-molecular-weight complexes are generally

in the range 10-15 $s^{-1}$ $mM^{-1}$ at magnetic field strengths 0.5-1.5 T and 298 K. This is considerably higher than the relaxivity of the classical CA GdDOTA under the same conditions ($r_1$ = 4-5 $s^{-1}$ $mM^{-1}$). Even higher relaxivities (30-40 $s^{-1}$ $mM^{-1}$) can be obtained by immobilization, for example by incorporation of mesoporous Mn(III)porphyrins in NMOFs.

The Mn(III) porphyrins have a preference for tumor tissue, which has been exploited for the development of many interesting CAs for MRI-guided therapy. The pharmacokinetics of Mn(III) porphyrins is dependent on their polarity. Hydrophilic systems like Mn(III)$TPPS_4$ and Mn(III)TCP are rapidly renally excreted, whereas hydrophobic complexes follow a preferential hepatic pathway and have longer residence times. Interesting cell-labeling has been achieved with esters of Mn(III)TCP, which appear to be taken up by cells, and once inside the cells they are hydrolyzed by esterases to the more hydrophilic carboxylates which cannot extravasate.

The toxicity of highly charged and hydrophilic Mn(III) porphyrins, like Mn(III)$TPPS_4$ and Mn(III)$T2EPyP^{5+}$, with fast PK and short tissue accumulation, is lower than for hydrophobic ones, such as $MnT2HexPyP^{5+}$, with wider biodistribution and higher brain accumulation. In animal studies, the difference between toxic and effective doses is moderate. Therefore, it is important to design systems with lower toxicity and/or higher efficiency.

The photothermic, photodynamic, and sonodynamic properties of porphyrins are preserved in the Mn(III)complexes, which have been exploited in the development of a variety of MRI CAs for MRI-guided therapies.

The perspectives for the clinical use of Mn(III) porphyrins as MRI contrast agents depend mostly on minimizing their *in vivo* toxicity at the doses required to produce observable contrast, which are about one order of magnitude higher that those used in radioprotection applications. As the full knowledge of the factors determining *in vivo* toxicity of Mn(III) porphyrins is still lacking, their administered dose could be significantly lowered by exploiting their natural concentration in tumors. Their application as CAs for MRI-guided therapies could also be further exploited, in particular for MRI-guided chemo, radiation and neutron capture therapy.

**Funding**

This research did not receive any specific grant from funding agencies in the public, commercial, or not-for-profit sectors.

**References**


[1] J. Wahsner, E.M. Gale, A. Rodríguez-Rodríguez, P. Caravan, Chemistry of MRI contrast agents: current challenges and new frontiers, Chem. Rev. 119 (2019) 957–1057. https://doi.org/10.1021/acs.chemrev.8b00363.

[2] A.E. Merbach, L. Helm, É. Tóth, The chemistry of contrast agents in medical magnetic resonance imaging, Second, John Wiley & Sons, Ltd, Chichester (UK), 2013. https://doi.org/10.1002/9781118503652.

[3] P. Caravan, J.J. Ellison, T.J. McMurry, R.B. Lauffer, Gadolinium(III) chelates as MRI contrast agents: structure, dynamics, and applications, Chem. Rev. 99 (1999) 2293–2352. https://doi.org/10.1021/cr980440x.

[4] V.C. Pierre, M.J. Allen, P. Caravan, Contrast agents for MRI: 30+ years and where are we going?, J. Biol. Inorg. Chem. 19 (2014) 127–131. https://doi.org/10.1007/s00775-013-1074-5.

[5] L. Helm, J.R. Morrow, C.J. Bond, F. Carniato, M. Botta, M. Braun, Z. Baranyai, R. Pujales-Paradela, M. Regueiro-Figueroa, D. Esteban-Gómez, C. Platas-Iglesias, T.J. Scholl, C. Pierre Valérie, M.J. Allen, Gadolinium-based contrast agents, in: C. Pierre Valérie, M.J. Allen (Eds.), New Dev. NMR, The Royal Society of Chemistry, London, 2018. https://doi.org/https://doi.org/10.1039/9781788010146-00121.

[6] A.G. Bleicher, E. Kanal, Assessment of adverse reaction rates to a newly approved MRI contrast agent: review of 23,553 administrations of gadobenate dimeglumine, Am. J. Roentgenol. 191 (2008) W307–W311. https://doi.org/10.2214/AJR.07.3951.

[7] E. Kanal, M.F. Tweedle, Residual or retained gadolinium: practical implications for radiologists and our patients, Radiology. 275 (2015) 630–634. https://doi.org/10.1148/radiol.2015150805.

[8] Z. Baranyai, E. Brücher, F. Uggeri, A. Maiocchi, I. Tóth, M. Andrási, A. Gáspár, L. Zékány, S. Aime, The role of equilibrium and kinetic properties in the dissociation of Gd[DTPA-bis(methylamide)] (Omniscan) at near to physiological conditions, Chem. Eur. J. 21 (2015) 4789–4799. https://doi.org/10.1002/chem.201405967.

[9] R. Pullicino, M. Radon, S. Biswas, M. Bhojak, K. Das, A review of the current evidence on gadolinium deposition in the brain, Clin. Neuroradiol. 28 (2018) 159–169. https://doi.org/10.1007/s00062-018-0678-0.

[10] A. Gupta, P. Caravan, W.S. Price, C. Platas-Iglesias, E.M. Gale, Applications for Transition-Metal Chemistry in Contrast-Enhanced Magnetic Resonance Imaging, Inorg. Chem. 59 (2020) 6648–6678. https://doi.org/10.1021/acs.inorgchem.0c00510.

[11] M. Botta, F. Carniato, D. Esteban-Gómez, C. Platas-Iglesias, L. Tei, Mn(II) compounds as an alternative to Gd-based MRI probes, Future Med. Chem. 11 (2019) 1461–1483. https://doi.org/10.4155/fmc-2018-0608.

[12] J. Wang, H. Wang, I. Ramsay, D.J. Erstad, B. Fuchs, K. Tanabe, P. Caravan, E.M. Gale, Manganese-Based Contrast Agents for Magnetic Resonance Imaging of Liver Tumors: Structure Activity Relationships and Lead Candidate Evaluation, J. Med. Chem. 61 (2018) 8811–8824. https://doi.org/10.1021/acs.jmedchem.8b00964.

[13] J.A. Peters, Relaxivity of manganese ferrite nanoparticles, Prog. Nucl. Magn. Reson. Spectrosc. 120–121 (2020) 72–94. https://doi.org/10.1016/j.pnmrs.2020.07.002.

[14] N.J. Patronas, J.S. Cohen, R.H. Knop, A.J. Dwyer, D. Colcher, J. Lundy, F. Mornex, P. Hambright, M. Sohn, C.E. Myers, Metalloporphyrin contrast agents for magnetic resonance imaging of human tumors in mice, Cancer Treat. Rep. 70 (1986) 391–395. PMID: 3955550.

[15] A.T.J. Klein, F. Roesch, H.H. Coenen, S.M. Qaim, Labelling of manganese-based magnetic resonance imaging (MRI) contrast agents with the positron emitter $^{51}$Mn, as exemplified by manganese-tetraphenyl-porphin-sulfonate ($MnTPPS_4$), Appl. Radiat. Isot. 62 (2005) 711–720. https://doi.org/10.1016/j.apradiso.2004.09.009.

[16] M.J.F. Calvete, S.M.A. Pinto, M.M. Pereira, C.F.G.C. Geraldes, Metal coordinated pyrrole-based macrocycles as contrast agents for magnetic resonance imaging technologies: Synthesis and applications, Coord. Chem. Rev. 333 (2017) 82–107. https://doi.org/10.1016/j.ccr.2016.11.011.

[17] K. Leung, C.J. Medforth, Ab initio molecular dynamics study of manganese porphine hydration and interaction with nitric oxide, Los Alamos Natl. Lab., Prepr. Arch., Condens. Matter. (2007) 1–10, arXiv:cond-mat/0701544.

[18] R.C. Lyon, P.J. Faustino, J.S. Cohen, A. Katz, F. Mornex, D. Colcher, C. Baglin, S.H. Koenig, P. Hambright, Tissue distribution and stability of metalloporphyrin MRI contrast agents, Magn. Reson. Med. 4 (1987) 24–33. https://doi.org/10.1002/mrm.1910040104.

[19] D. Zhang, W. Lan, Z. Zhou, L. Yang, Q. Liu, Y. Bian, J. Jiang, Manganese(III) Porphyrin-Based Magnetic Materials, Top. Curr. Chem. 377 (2019) 18. https://doi.org/10.1007/s41061-019-0244-5.

[20] B. Cheng, F. Cukiernik, P.H. Fries, J.-C. Marchon, W.R. Scheidt, A Novel Dimanganese(III) Complex with a Single Hydroxo Bridge. Syntheses, Structures, and Magnetic Susceptibilities of μ-Hydroxo)bis((octaethylporphinato)manganese(III)) Perchlorate and a Monomeric Precursor, Aquo(octaethylporphinato)manganese(III) Perchlorate, Inorg. Chem. 34 (1995) 4627–4639. https://doi.org/10.1021/ic00122a020.

[21] I. Batinic-Haberle, A. Tovmasyan, I. Spasojevic, Mn Porphyrin-Based Redox-Active Drugs: Differential Effects as Cancer Therapeutics and Protectors of Normal Tissue Against Oxidative Injury, Antioxid. Redox Signal. 29 (2018) 1691–1724. https://doi.org/10.1089/ars.2017.7453.

[22] M.N. Williamson, C.L. Hill, Molecular stereochemistry of aquamanganese(III) porphyrins. Demonstrable effect of π-arene-porphyrin interaction in the metal coordination environment in the metalloporphyrin, Inorg. Chem. 26 (1987) 4155–4160. https://doi.org/10.1021/ic00272a005.

[23] C.-W. Chen, J.S. Cohen, C.E. Myers, M. Sohn, Paramagnetic metalloporphyrins as potential contrast agents in NMR imaging, FEBS Lett. 168 (1984) 70–74. https://doi.org/http://dx.doi.org/10.1016/0014-5793(84)80208-2.

[24] R.J. Fiel, T.M. Button, S. Gilani, E.H. Mark, D.A. Musser, R.M. Henkelman, M.J. Bronskill, J.G. Van Heteren, Proton relaxation enhancement by manganese(III)$TPPS_4$ in a model tumor system, Magn. Reson. Imaging. 5 (1987) 149–156. https://doi.org/10.1016/0730-725X(87)90044-0.

[25] S.H. Koenig, R.D. Brown, M. Spiller, The anomalous relaxivity of $Mn^{3+}(TPPS_4)$, Magn. Reson. Med. 4 (1987) 252–260. https://doi.org/10.1002/mrm.1910040306.

[26] T.M. Button, R.J. Fiel, Isointense model for the evaluation of tumor-specific MRI contrast agents, Magn. Reson. Imaging. 6 (1988) 275–280. https://doi.org/10.1016/0730-

725X(88)90402-X.

[27] P. Furmanski, C. Longley, Metalloporphyrin enhancement of magnetic resonance imaging of human tumor xenografts in nude mice, Cancer Res. 48 (1988) 4604–4610. http://cancerres.aacrjournals.org/cgi/content/abstract/48/16/4604.

[28] R.J. Fiel, D.A. Musser, E.H. Mark, R. Mazurchuk, J.J. Alletto, A comparative study of manganese meso-sulfonatophenyl porphyrins: contrast-enhancing agents for tumors, Magn. Reson. Imaging. 8 (1990) 255–259. https://doi.org/10.1016/0730-725X(90)90097-L.

[29] G. Hernández, R.G. Bryant, Proton magnetic relaxation of manganese(II) tetrakis(4-sulfophenyl)porphine ion in water, Bioconjugate Chem. 2 (1991) 394–397. https://doi.org/10.1021/bc00012a002.

[30] A. Harriman, G. Porter, Photochemistry of manganese porphyrins. Part 1.-Characterisation of some water soluble complexes, J. Chem. Soc. Faraday Trans. 2 Mol. Chem. Phys. 75 (1979) 1532–1542. https://doi.org/10.1039/F29797501532.

[31] T.J. Swift, R.E. Connick, NMR (nuclear magnetic resonance)-relaxation mechanisms of O-17 in aqueous solutions of paramagnetic cations and the lifetime of water molecules in the first coordination sphere, J. Chem. Phys. 37 (1962) 307–320. https://doi.org/10.1063/1.1701321

[32] J.S. Leigh Jr., Relaxation times in systems with chemical exchange: Some exact solutions, J. Magn. Reson. 4 (1971) 308–311. https://doi.org/10.1016/0022-2364(71)90040-0.

[33] N. Schaefle, R. Sharp, NMR Paramagnetic Relaxation of the Spin 2 Complex $Mn^{III}$TSPP: A Unique Mechanism, J. Phys. Chem. A. 109 (2005) 3267–3275. https://doi.org/10.1021/jp046227o.

[34] I. Bertini, C. Luchinat, G. Parigi, E. Ravera, NMR of Paramagnetic Molecules, 2nd ed, Elsevier, Amsterdam, 2017. https://doi.org/10.1016/b978-0-444-63436-8.00022-3.

[35] A. Budimir, J. Kalmar, I. Fabian, G. Lente, I. Banyai, I. Batinic-Haberle, M. Birus, Water exchange rates of water-soluble manganese(III) porphyrins of therapeutical potential, Dalton Trans. 39 (2010) 4405–4410. https://doi.org/10.1039/b926522h.

[36] H. Liu, W. Cheng, S. Dong, D.F. Xu, K. Tang, X.-A. Zhang, A Second Generation Mn-Porphyrin Dimer with a Twisted Linker as a Potential Blood Pool Agent for MRI: Tuning the Geometry and Binding with HSA, Pharmaceuticals. 13 (2020) 282. https://doi.org/10.3390/ph13100282.

[37] S. Aime, M. Botta, E. Gianolio, E. Terreno, A p(O-2)-responsive MRI contrast agent based on the redox switch of manganese(II/III) - Porphyrin complexes, Angew. Chem. Int. Ed. Engl. 39 (2000) 747–750. https://doi.org/10.1002/(SICI)1521-3773(20000218)39:4<747::AID-ANIE747>3.0.CO;2-2.

[38] S.K. Saini, A. Jena, J. Dey, A.K. Sharma, R. Singh, $MnPcS_4$: a new MRI contrast enhancing agent for tumor localization in mice, Magn. Reson. Imaging. 13 (1995) 985–990. https://doi.org/10.1016/0730-725X(95)00046-J.

[39] D.H. Powell, O.M. Ni Dhubhghaill, D. Pubanz, L. Helm, Y.S. Lebedev, W. Schlaepfer, A.E. Merbach, High-pressure NMR kinetics. Part 74. Structural and dynamic parameters obtained from O-17 NMR, EPR, and NMRD studies of monomeric and dimeric $Gd^{3+}$ complexes of interest in magnetic resonance imaging: An integrated and theoretically self consistent approac, J. Am. Chem. Soc. 118 (1996) 9333–9346. https://doi.org/10.1021/ja961743g.

[40] K.E. Kellar, N. Foster, Relaxation enhancement of water protons by manganese(III) porphyrins: influence of porphyrin aggregation, Inorg. Chem. 31 (1992) 1353–1359.

https://doi.org/10.1021/ic00034a012.

[41] L.H. Bryant Jr., M.W. Hodges, R.G. Bryant, Test of Electron Delocalization Effects on Water-Proton Spin-Lattice Relaxation by Bromination of [Tetrakis(4-sulfonatopheny)porphine]manganese, Inorg. Chem. 38 (1999) 1002–1005. https://doi.org/10.1021/IC981197N.

[42] N. Sahoo, T.P. Das, Theory of hyperfine interactions in aqueous manganese(3+)-porphyrin system, Hyperfine Interact. 61 (1990) 1197–1200. https://doi.org/10.1007/BF02407601.

[43] G.A. Mercier, On the molecular spin density and the electrostatic potential as determinants of the relaxivity of metalloporphyrins., Magn. Reson. Imaging. 13 (1995) 807–817. https://doi.org/10.1016/0730-725X(95)00038-I.

[44] G.A. Mercier Jr., Enhancing the relaxivity of paramagnetic coordination complexes through the optimization of the molecular electrostatic potential, Magn. Reson. Imaging. 16 (1998) 811–828. https://doi.org/10.1016/S0730-725X(98)00087-3.

[45] L.H. Bryant Jr., G.A. Mercier Jr., Relaxometric investigations of functional group placement on MnTPP derivatives supports the role of the molecular electrostatic potential maps as a tool to design new metalloporphyrins with larger relaxivities., Int. J. Mol. Sci. [Online Comput. File]. 2 (2001) 140–147. https://doi.org/10.3390/i2030140.

[46] R.-J. Cheng, S.-H. Chang, K.-C. Hung, An Anomalous Spin-Polarization Mechanism in High-Spin Manganese(III) Porphyrin Complexes, Inorg. Chem., 46 (2007) 1948-1950. https://doi.org/10.1021/ic0617238.

[47] J. Krzystek, J. Telser, High frequency and field EPR spectroscopy of Mn(III) complexes in frozen solutions, J. Magn. Reson. 162 (2003) 454–465. https://doi.org/https://doi.org/10.1016/S1090-7807(03)00042-9.

[48] E. Belorizky, P.H. Fries, L. Helm, J. Kowalewski, D. Kruk, R.R. Sharp, P.O. Westlund, Comparison of different methods for calculating the paramagnetic relaxation enhancement of nuclear spins as a function of the magnetic field, J. Chem. Phys. 128 (2008) 52315. https://doi.org/10.1063/1.2833957.

[49] S.M. Abernathy, J.C. Miller, L.L. Lohr, R.R. Sharp, Nuclear magnetic resonance-paramagnetic relaxation enhancements: Influence of spatial quantization of the electron spin when the zero-field splitting energy is larger than the Zeeman energy, J. Chem. Phys. 109 (1998) 4035–4046. https://doi.org/10.1063/1.477003.

[50] I.E. Haedicke, T. Li, Y.L.K. Zhu, F. Martinez, A.M. Hamilton, D.H. Murrell, J.T. Nofiele, H.-L.M. Cheng, T.J. Scholl, P.J. Foster, X. Zhang, An enzyme-activatable and cell-permeable $Mn^{III}$-porphyrin as a highly efficient $T_1$ MRI contrast agent for cell labeling, Chem. Sci. 7 (2016) 4308–4317. https://doi.org/10.1039/C5SC04252F.

[51] S.M.A. Pinto, M.J.F. Calvete, M.E. Ghica, S. Soler, I. Gallardo, A. Pallier, M.B. Laranjo, A.M.S. Cardoso, M.M.C.A. Castro, C.M.A. Brett, M.M. Pereira, E. Tóth, C.F.G.C. Geraldes, A biocompatible redox MRI probe based on a Mn(II)/Mn(II) porphyrin, Dalton Trans. 48 (2019) 3249–3262. https://doi.org/10.1039/c8dt04775h.

[52] H.-S. Lu, M.-Y. Wang, F.-P. Ying, Y.-Y. Lv, Manganese(III) porphyrin oligomers as high-relaxivity MRI contrast agents, Bioorg. Med. Chem. 35 (2021) 116090. https://doi.org/10.1016/j.bmc.2021.116090.

[53] S.K. Sur, R.G. Bryant, Spin-lattice relaxation enhancement of water protons by manganese porphyrins complexed with cyclodextrins, J. Phys. Chem. 99 (1995) 4900–4905.

https://doi.org/10.1021/j100014a005.

[54] J.E. Bradshaw, K.A. Gillogly, L.J. Wilson, K. Kumar, X. Wan, M.F. Tweedle, G. Hernandez, R.G. Bryant, New non-ionic water-soluble porphyrins: evaluation of manganese(III) polyhydroxylamide porphyrins as MRI contrast agents, Inorg. Chim. Acta. 275–276 (1998) 106–116. https://doi.org/10.1016/S0020-1693(97)06110-0.

[55] W. Cheng, T. Ganesh, F. Martinez, J. Lam, H. Yoon, R.B. MacGregor Jr., T.J. Scholl, H.-L.M. Cheng, X. Zhang, Binding of a dimeric manganese porphyrin to serum albumin: towards a gadolinium-free blood-pool $T_1$ MRI contrast agent, J. Biol. Inorg. Chem. 19 (2014) 229–235. https://doi.org/10.1007/s00775-013-1073-6.

[56] W. Cheng, I.E. Haedicke, J. Nofiele, F. Martinez, K. Beera, T.J. Scholl, H.-L.M. Cheng, X. Zhang, Complementary Strategies for Developing Gd-Free High-Field $T_1$ MRI Contrast Agents Based on $Mn^{III}$ Porphyrins, J. Med. Chem. 57 (2014) 516–520. https://doi.org/10.1021/jm401124b.

[57] H.-L.M. Cheng, I.E. Haedicke, W. Cheng, N.J. Tchouala, X. Zhang, Gadolinium-free $T_1$ contrast agents for MRI: tunable pharmacokinetics of a new class of manganese porphyrins, J. Magn. Reson. Imaging. 40 (2014) 1474–1480. https://doi.org/10.1002/jmri.24483.

[58] J.T. Nofiele, I.E. Haedicke, Y.L.K. Zhu, X. Zhang, H.-L.M. Cheng, Gadolinium-free extracellular MR contrast agent for tumor imaging, J. Magn. Reson. Imaging. 41 (2015) 397–403. https://doi.org/10.1002/jmri.24561.

[59] G. Marchal, Y. Ni, P. Herijgers, W. Flameng, C. Petre, H. Bosmans, J. Yu, W. Ebert, C.S. Hilger, D. Pfefferer, W. Semmler, A.L. Baert, Paramagnetic metalloporphyrins: infarct avid contrast agents for diagnosis of acute myocardial infarction by MRI, Eur. Radiol. 6 (1996) 2–8. https://doi.org/10.1007/BF00619942.

[60] X. Zheng, J. Qian, F. Tang, Z. Wang, C. Cao, K. Zhong, Microgel-Based Thermosensitive MRI Contrast Agent, ACS Macro Lett. 4 (2015) 431–435. https://doi.org/10.1021/acsmacrolett.5b00058.

[61] M. Sun, H.-Y. Zhang, B.-W. Liu, Y. Liu, Construction of a Supramolecular Polymer by Bridged Bis(permethyl-β-cyclodextrin)s with Porphyrins and Its Highly Efficient Magnetic Resonance Imaging, Macromolecules. 46 (2013) 4268–4275. https://doi.org/10.1021/ma400806s.

[62] Y. Ni, G. Marchal, J. Yu, G. Lukito, C. Petre, M. Wevers, A.L. Baert, W. Ebert, C.S. Hilger, F.K. Maier, Localization of metalloporphyrin-induced “specific” enhancement in experimental liver tumors: comparison of magnetic resonance imaging, microangiographic, and histologic findings, Acad. Radiol. 2 (1995) 687–699. https://doi.org/10.1016/S1076-6332(05)80437-4.

[63] M. Alhamami, W. Cheng, Y. Lyu, C. Allen, X. Zhang, H.-L.M. Cheng, Manganese-porphyrin-enhanced MRI for the detection of cancer cells: a quantitative in vitro investigation with multiple clinical subtypes of breast cancer, PLoS One. 13 (2018) e0196998/1-e0196998/17. https://doi.org/10.1371/journal.pone.0196998.

[64] X. Liu, G. Yang, L. Zhang, Z. Liu, Z. Cheng, X. Zhu, Photosensitizer cross-linked nano-micelle platform for multimodal imaging guided synergistic photothermal/photodynamic therapy, Nanoscale. 8 (2016) 15323–15339. https://doi.org/10.1039/C6NR04835H.

[65] M. He, Y. Chen, C. Tao, Q.Q. Tian, L. An, J. Lin, Q.Q. Tian, H. Yang, S. Yang, Mn-Porphyrin-Based Metal-Organic Framework with High Longitudinal Relaxivity for Magnetic Resonance Imaging Guidance and Oxygen Self-Supplementing Photodynamic Therapy, ACS Appl. Mater. Interfaces. 11 (2019) 41946–41956. https://doi.org/10.1021/acsami.9b15083.

[66] L. Jing, X. Liang, X. Li, Y. Yang, Z. Dai, Covalent attachment of Mn-porphyrin onto doxorubicin-loaded poly(lactic acid) nanoparticles for potential magnetic resonance imaging and pH-sensitive drug delivery, Acta Biomater. 9 (2013) 9434–9441. https://doi.org/10.1016/j.actbio.2013.08.018.

[67] T. Zou, M. Zhen, D. Chen, R. Li, M. Guan, C. Shu, H. Han, C. Wang, The positive influence of fullerene derivatives bonded to manganese(III) porphyrins on water proton relaxation, Dalton Trans. 44 (2015) 9114–9119. https://doi.org/10.1039/C4DT03482A.

[68] Z. Zhang, R. He, K. Yan, Q. ni Guo, Y. guo Lu, X. xia Wang, H. Lei, Z. ying Li, Synthesis and in vitro and in vivo evaluation of manganese(III) porphyrin-dextran as a novel MRI contrast agent, Bioorganic Med. Chem. Lett. 19 (2009) 6675–6678. https://doi.org/10.1016/j.bmcl.2009.10.003.

[69] L. Jing, X. Liang, X. Li, L. Lin, Y. Yang, X. Yue, Z. Dai, Mn-porphyrin conjugated Au nanoshells encapsulating doxorubicin for potential magnetic resonance imaging and light triggered synergistic therapy of cancer, Theranostics. 4 (2014) 858–871. https://doi.org/10.7150/thno.8818.

[70] X. Liang, X. Li, L. Jing, X. Yue, Z. Dai, Theranostic porphyrin dyad nanoparticles for magnetic resonance imaging guided photodynamic therapy, Biomaterials. 35 (2014) 6379–6388. https://doi.org/10.1016/j.biomaterials.2014.04.094.

[71] Y. Hitomi, T. Ekawa, M. Kodera, Water proton relaxivity, superoxide dismutase-like activity, and cytotoxicity of a manganese(III) porphyrin having four poly(ethylene glycol) tails, Chem. Lett. 43 (2014) 732–734. https://doi.org/10.1246/cl.140029.

[72] K. Choi, D.-H. Lee, W.-D. Jang, Supramolecular micelle from amphiphilic Mn(III)-porphyrin derivatives as a potential MRI contrast agent, Bull. Korean Chem. Soc. 31 (2010) 639–644. https://doi.org/10.5012/bkcs.2010.31.03.639.

[73] K.E. Kellar, S.M. Spaltro, N. Foster, Determination of the residence lifetimes of water molecules in the inner coordination sphere of paramagnetic metalloporphyrins and their adducts with poly(α-amino acids), Macromolecules. 23 (1990) 428–431. https://doi.org/10.1021/ma00204a013.

[74] V. Mouraviev, T.N. Venkatraman, A. Tovmasyan, M. Kimura, M. Tsivian, V. Mouravieva, T.J. Polascik, H. Wang, T.J. Amrhein, I. Batinic-Haberle, C. Lascola, Mn porphyrins as novel molecular magnetic resonance imaging contrast agents, J. Endourol. 26 (2012) 1420–1424. https://doi.org/10.1089/end.2012.0171.

[75] I.G. Meerovich, M. V Gulyaev, G.A. Meerovich, M.S. Belov, V.M. Derkacheva, O. V Dolotova, V.B. Loschenov, A.Y. Baryshnikov, Y.A. Pirogov, Study of phthalocyanine derivatives as contrast agents for magnetic resonance imaging, Russ. J. Gen. Chem. 85 (2015) 333–337. https://doi.org/10.1134/S1070363215010478.

[76] S.M.A. Pinto, V.A. Tomé, M.M. Pereira, H.D. Burrows, M.J.F. Calvete, A.M.S. Cardoso, A. Pallier, É. Tóth, M.M.C.A. Castro, C.F.G.C. Geraldes, The quest for biocompatible phthalocyanines for molecular imaging: Photophysics, relaxometry and cytotoxicity studies, J. Inorg. Biochem. 154 (2016) 50–59. https://doi.org/10.1016/j.jinorgbio.2015.10.013.

[77] S.M. Spaltro, N. Foster, Synthesis and characterization of conjugates of poly(α-amino acids) and manganese(III) protoporphyrin IX as relaxation enhancement agents for MRI, J. Appl. Polym. Sci. 41 (1990) 1235–1249. https://doi.org/10.1002/app.1990.070410532.

[78] D. Pan, A.H. Schmieder, S.A. Wickline, G.M. Lanza, Manganese-based MRI contrast agents:

past, present, and future, Tetrahedron. 67 (2011) 8431–8444. https://doi.org/10.1016/j.tet.2011.07.076.

[79] D. Pan, S.D. Caruthers, A. SenPan, A.H. Schmieder, T.A. Williams, M.J. Scott, P.J. Gaffney, S.A. Wickline, G. Lanza, Thrombus-specific manganese-based “nanobialys” for MR molecular imaging of ruptured plaque, J. Cardiovasc. Magn. Reson. 14 (2012) P136–P136. https://doi.org/10.1186/1532-429X-14-S1-P136.

[80] R.K. Gupta, A.S. Mildvan, G.R. Schonbaum, Water proton relaxation studies of the heme-environment in Mn(III)-substituted and native horseradish peroxidases, Arch. Biochem. Biophys. 202 (1980) 1–7. https://doi.org/https://doi.org/10.1016/0003-9861(80)90398-7.

[81] M.B. Winter, P.J. Klemm, C.M. Phillips-Piro, K.N. Raymond, M.A. Marletta, Porphyrin-Substituted H-NOX Proteins as High-Relaxivity MRI Contrast Agents, Inorg. Chem. 52 (2013) 2277–2279. https://doi.org/10.1021/ic302685h.

[82] V.S. Lelyveld, E. Brustad, F.H. Arnold, A. Jasanoff, Metal-Substituted Protein MRI Contrast Agents Engineered for Enhanced Relaxivity and Ligand Sensitivity, J. Am. Chem. Soc. 133 (2011) 649–651. https://doi.org/10.1021/ja107936d.

[83] S. Qazi, M. Uchida, R. Usselman, R. Shearer, E. Edwards, T. Douglas, Manganese(III) porphyrins complexed with P22 virus-like particles as $T_1$-enhanced contrast agents for magnetic resonance imaging, JBIC, J. Biol. Inorg. Chem. 19 (2014) 237–246. https://doi.org/10.1007/s00775-013-1075-4.

[84] P. Poulet, M. Ouzafe, J. Steibel, Y. Mauss, J. Chambron, Hematoporphyrin-manganese: a contrast agent for tumors in magnetic resonance imaging, NATO ASI Ser., Ser. H. 15 (1988) 97–99. https://doi.org/10.1007/978-3-642-73151-8_14.

[85] I.G. Meerovich, A. Brandis, G.A. Meerovich, A.A. Stratonnikov, P. Bendel, N.A. Oborotova, A. Shertz, A.Y. Baryshnikov, Study of manganese bacteriopheophorbide as a potential contrast agent for magnetic resonance tomography, Bull. Exp. Biol. Med. 143 (2007) 452–454. https://doi.org/10.1007/s10517-007-0154-3.

[86] T.D. MacDonald, T.W. Liu, G. Zheng, An MRI-sensitive, non-photobleachable Porphysome photothermal agent, Angew. Chem., Int. Ed. 53 (2014) 6956–6959. https://doi.org/10.1002/anie.201400133.

[87] S. Shao, T.N. Do, A. Razi, U. Chitgupi, J. Geng, R.J. Alsop, B.G. Dzikovski, M.C. Rheinstädter, J. Ortega, M. Karttunen, J.A. Spernyak, J.F. Lovell, Design of Hydrated Porphyrin-Phospholipid Bilayers with Enhanced Magnetic Resonance Contrast, Small. 13 (2017) 1602505. https://doi.org/10.1002/smll.201602505.

[88] D.H. Robinson, U.P. Schmiedl, F.L. Starr, J.A. Nelson, R. Malek, Intravenous manganese-mesoporphyrin as a magnetic resonance imaging contrast agent: an experimental model using VX-2 carcinoma in rabbits, Acad. Radiol. 2 (1995) 43–49. https://doi.org/10.1016/s1076-6332(05)80245-4.

[89] U.P. Schmiedl, J.A. Nelson, F.L. Starr, R. Schmidt, Hepatic contrast-enhancing properties of manganese-mesoporphyrin and manganese-$TPPS_4$. A comparative magnetic resonance imaging study in rats, Invest. Radiol. 27 (1992) 536–542. https://doi.org/10.1097/00004424-199207000-00013

[90] J.H. McMillan, G.G. Cox, B.F. Kimler, J.S. Spicer, S. Batnitzky, Manganese uroporphyrin I: a novel metalloporphyrin contrast agent for magnetic resonance imaging, Magn. Reson. Imaging. 9 (1991) 553–558. https://doi.org/10.1016/0730-725X(91)90042-K.

[91] L.R. Huang, R.M. Straubinger, S.B. Kahl, M.-S. Koo, J.J. Alletto, R. Mazurchuk, R.I. Chau, S.L. Thamer, R.J. Fiel, Boronated Metalloporphyrins: A novel approach to the diagnosis and treatment of cancer using contrast-enhanced MR imaging and neutron capture therapy, J. Magn. Reson. Imaging. 3 (1993) 351–356. https://doi.org/https://doi.org/10.1002/jmri.1880030210.

[92] L. Helm, A.E. Merbach, Inorganic and Bioinorganic Solvent Exchange Mechanisms, Chem. Rev. 105 (2005) 1923–1959. https://doi.org/10.1021/cr030726o.

[93] D. Lieb, A. Zahl, T.E. Shubina, I. Ivanović-Burmazović, Water Exchange on Manganese(III) Porphyrins. Mechanistic Insights Relevant for Oxygen Evolving Complex and Superoxide Dismutation Catalysis, J. Am. Chem. Soc. 132 (2010) 7282–7284. https://doi.org/10.1021/ja1014585.

[94] L. Helm, A.E. Merbach, The Periodic Table and Kinetics?, Chimia. 73 (2019) 179–184. https://doi.org/10.2533/chimia.2019.179.

[95] A.D. Sherry, R.D. Brown, C.F.G.C. Geraldes, S.H. Koenig, K.-T. Kuan, M. Spiller, Synthesis and characterization of the gadolinium(3+) complex of DOTA-propylamide: a model DOTA-protein conjugate, Inorg. Chem. 28 (1989) 620–622. https://doi.org/10.1021/ic00302a049.

[96] S. Aime, P.L. Anelli, M. Botta, F. Fedeli, M. Grandi, P. Paoli, F. Uggeri, Synthesis, characterization, and 1/T1 NMRD profiles of gadolinium(III) complexes of monoamide derivatives of DOTA-like ligands. X-ray structure of the 10-[2-[[2-hydroxy-1-(hydroxymethyl)ethyl]amino]-1-[(phenylmethoxy)methyl]-2-oxoethyl]-1,4,7,10-tetraazac, Inorg. Chem. 31 (1992) 2422–2428. https://doi.org/10.1021/ic00038a023.

[97] S. Aime, M. Botta, G. Ermondi, F. Fedeli, F. Uggeri, Synthesis and NMRD studies of gadolinium(3+) complexes of macrocyclic polyamino polycarboxylic ligands bearing .beta.-benzyloxy-.alpha.-propionic residues, Inorg. Chem. 31 (1992) 1100–1103. https://doi.org/10.1021/ic00032a035.

[98] V.E. Yushmanov, H. Imasato, T.T. Tominaga, M. Tabak, 1H NMR and electronic absorption spectroscopy of paramagnetic water-soluble meso-tetraarylsubstituted cationic and anionic metalloporphyrins, J. Inorg. Biochem. 61 (1996) 233–250. https://doi.org/10.1016/0162-0134(95)00071-2.

[99] V.E. Yushmanov, T.T. Tominaga, I.E. Borissevitch, H. Imasato, M. Tabak, Binding of manganese and iron tetraphenylporphine sulfonates to albumin is relevant to their contrast properties, Magn. Reson. Imaging. 14 (1996) 255–261. https://doi.org/10.1016/0730-725X(95)02103-Z.

[100] D. Pan, S.D. Caruthers, G. Hu, A. Senpan, M.J. Scott, P.J. Gaffney, S.A. Wickline, G.M. Lanza, Ligand-Directed Nanobialys as Theranostic Agent for Drug Delivery and Manganese-Based Magnetic Resonance Imaging of Vascular Targets, J. Am. Chem. Soc. 130 (2008) 9186–9187. https://doi.org/10.1021/ja801482d.

[101] D. Pan, S.D. Caruthers, A. Senpan, A.H. Schmieder, S.A. Wickline, G.M. Lanza, Revisiting an old friend: manganese-based MRI contrast agents, Wiley Interdiscip. Rev. Nanomed. Nanobiotechnol. 3 (2011) 162–173. https://doi.org/10.1002/wnan.116.

[102] H. Zhang, X.-T. Tian, Y. Shang, Y.-H. Li, X.-B. Yin, Theranostic Mn-Porphyrin Metal-Organic Frameworks for Magnetic Resonance Imaging-Guided Nitric Oxide and Photothermal Synergistic Therapy, ACS Appl. Mater. Interfaces. 10 (2018) 28390–28398. https://doi.org/10.1021/acsami.8b09680.

[103] K. Bockhorst, M. Höhn-Berlage, M. Kocher, K.A. Hossmann, Proton relaxation enhancement in

experimental brain tumors—In vivo NMR study of manganese(III)TPPS in rat brain gliomas, Magn. Reson. Imaging. 8 (1990) 499–504. https://doi.org/https://doi.org/10.1016/0730-725X(90)90058-A.

[104] Y. Ni, C. Petre, Y. Miao, J. Yu, E. Cresens, P. Adriaens, H. Bosmans, W. Semmler, A.L. Baert, G. Marchal, Magnetic resonance imaging-histomorphologic correlation studies on paramagnetic metalloporphyrins in rat models of necrosis, Invest. Radiol. 32 (1997) 770–779. https://doi.org/10.1097/00004424-199712000-00008.

[105] Y. Takehara, H. Sakahara, H. Masunaga, S. Isogai, N. Kodaira, H. Takeda, T. Saga, S. Nakajima, I. Sakata, Tumour enhancement with newly developed Mn-metalloporphyrin (HOP-9P) in magnetic resonance imaging of mice, Br. J. Cancer. 84 (2001) 1681–1685. https://doi.org/10.1054/bjoc.2001.1802.

[106] Y. Takehara, H. Sakahara, H. Masunaga, S. Isogai, N. Kodaira, M. Sugiyama, H. Takeda, T. Saga, S. Nakajima, I. Sakata, Assessment of a potential tumor-seeking manganese metalloporphyrin contrast agent in a mouse model, Magn. Reson. Med. 47 (2002) 549–553. https://doi.org/10.1002/mrm.10109.

[107] H. Nasu, Y. Takehara, S. Isogai, N. Kodaira, H. Takeda, T. Saga, S. Nakajima, I. Sakata, H. Sakahara, Tumor enhancement using Mn-metalloporphyrin in mice: Magnetic resonance imaging and histopathologic correlation, J. Magn. Reson. Imaging. 20 (2004) 294–299. https://doi.org/10.1002/jmri.20112.

[108] M. Chen, X. Liang, Z. Dai, Manganese(iii)-chelated porphyrin microbubbles for enhanced ultrasound/MR bimodal tumor imaging through ultrasound-mediated micro-to-nano conversion, Nanoscale 11 (2019) 10178–10182. https://doi.org/10.1039/C9NR01373C.

[109] I. Batinic-Haberle, A. Tovmasyan, I. Spasojevic, An educational overview of the chemistry, biochemistry and therapeutic aspects of Mn porphyrins - From superoxide dismutation to H2O2-driven pathways, Redox Biol. 5 (2015) 43–65. https://doi.org/10.1016/j.redox.2015.01.017.

[110] S.L. O'Neal, W. Zheng, Manganese Toxicity Upon Overexposure: a Decade in Review, Curr. Environ. Health Rep. 2 (2015) 315–328. https://doi.org/10.1007/s40572-015-0056-x.

[111] H.M.F. Tieu, X. Zhang, Redox Behaviour and Stability of Manganese Porphyrins Based MRI Contrast Agents, MSc Thesis, University of Toronto, 2018.

[112] M.D. Ogan, D. Revel, R.C. Brasch, Metalloporphyrin Contrast Enhancement of Tumors in Magnetic Resonance Imaging A Study of Human Carcinoma, Lymphoma, and Fibrosarcoma in Mice, Invest. Radiol. 22 (1987) 822–828. https://doi.org/10.1097/00004424-198710000-00009.

[113] D.A. Place, P.J. Faustino, P.C.M. Van Zijl, A. Chesnick, J.S. Cohen, Metalloporphyrins as contrast agents for tumors in magnetic resonance imaging, Invest. Radiol. 25 (1990) S69–S70. https://doi.org/10.1097/00004424-199009001-00033.

[114] L.S. Jackson, J.A. Nelson, T.A. Case, B.F. Burnham, Manganese protoporphyrin IX. A potential intravenous paramagnetic NMR contrast agent: preliminary communication, Invest. Radiol. 20 (1985) 226–229. https://doi.org/10.1097/00004424-198503000-00024.

[115] B.J. Moeller, I. Batinic-Haberle, I. Spasojevic, Z.N. Rabbani, M.S. Anscher, Z. Vujaskovic, M.W. Dewhirst, A manganese porphyrin superoxide dismutase mimetic enhances tumor radioresponsiveness, Int. J. Radiat. Oncol. Biol. Phys. 63 (2005) 545–552. https://doi.org/10.1016/j.ijrobp.2005.05.026.

[116] S.C. Gad, D.W. Sullivan, J.D. Crapo, C.B. Spainhour, A Nonclinical Safety Assessment of MnTE-2-PyP, a Manganese Porphyrin, Int. J. Toxicol. 32 (2013) 274–287. https://doi.org/10.1177/1091581813490203.

[117] S. Loai, I. Haedicke, Z. Mirzaei, C.A. Simmons, X. Zhang, H.-L.M. Cheng, Positive-contrast cellular MRI of embryonic stem cells for tissue regeneration using a highly efficient T1 MRI contrast agent, J. Magn. Reson. Imaging 44 (2016) 1456-1463. https://doi.org/10.1002/jmri.25299.

[118] I.E. Haedicke, S. Loai, H.-L.M. Cheng, An efficient T1 contrast agent for labeling and tracking human embryonic stem cells on MRI, Contrast Media Mol. Imaging. (2019) 3475786. https://doi.org/10.1155/2019/3475786.

[119] A. Venter, D.A. Szulc, S. Loai, T. Ganesh, I.E. Haedicke, H.-L.M. Cheng, A manganese porphyrin-based T1 contrast agent for cellular MR imaging of human embryonic stem cells, Sci. Rep. 8 (2018) 1–11. https://doi.org/10.1038/s41598-018-30661-w.

[120] G.S. Loving, S. Mukherjee, P. Caravan, Redox-Activated Manganese-Based MR Contrast Agent, J. Am. Chem. Soc. 135 (2013) 4620–4623. https://doi.org/10.1021/ja312610j.

[121] X. Zhang, K.S. Lovejoy, A. Jasanoff, S.J. Lippard, Water-soluble porphyrins as a dual-function molecular imaging platform for MRI and fluorescence zinc sensing, Proc. Natl. Acad. Sci. U. S. A. 104 (2007) 10780–10785. https://doi.org/10.1073/pnas.0702393104.

[122] T. Lee, X. Zhang, S. Dhar, H. Faas, S.J. Lippard, A. Jasanoff, In Vivo Imaging with a Cell-Permeable Porphyrin-Based MRI Contrast Agent, Chem. Biol. 17 (2010) 665–673. https://doi.org/https://doi.org/10.1016/j.chembiol.2010.05.009.

[123] G.G. Westmeyer, Y. Emer, J. Lintelmann, A. Jasanoff, MRI-Based Detection of Alkaline Phosphatase Gene Reporter Activity Using a Porphyrin Solubility Switch, Chem. Biol. (Oxford, U. K.). 21 (2014) 422–429. https://doi.org/10.1016/j.chembiol.2014.01.012.

[124] J.M. Keca, J. Chen, M. Overchuk, N. Muhanna, C.M. MacLaughlin, C.S. Jin, W.D. Foltz, J.C. Irish, G. Zheng, Nanotexaphyrin: One-Pot Synthesis of a Manganese Texaphyrin-Phospholipid Nanoparticle for Magnetic Resonance Imaging, Angew. Chemie Int. Ed. 55 (2016) 6187–6191. https://doi.org/10.1002/anie.201600234.

[125] J.F. Lovell, C.S. Jin, E. Huynh, H. Jin, C. Kim, J.L. Rubinstein, W.C.W. Chan, W. Cao, L. V Wang, G. Zheng, Porphysome nanovesicles generated by porphyrin bilayers for use as multimodal biophotonic contrast agents, Nat. Mater. 10 (2011) 324–332. https://doi.org/10.1038/nmat2986.

[126] D. Feng, Z.-Y. Gu, Y.-P. Chen, J. Park, Z. Wei, Y. Sun, M. Bosch, S. Yuan, H.-C. Zhou, A Highly Stable Porphyrinic Zirconium Metal–Organic Framework with shp-a Topology, J. Am. Chem. Soc. 136 (2014) 17714–17717. https://doi.org/10.1021/ja510525s.

[127] J. Bao, X. Wang, Y. Shi, J. Cheng, J. Bao, X. Zu, J. Li, D. Fan, Q. Xia, Multifunctional Hf/Mn-TCPP Metal-Organic Framework Nanoparticles for Triple-Modality Imaging-Guided PTT/RT Synergistic Cancer Therapy, Int. J. Nanomed. 15 (2020) 7687–7702. doi: 10.2147/IJN.S267321.

[128] K.A. Ashcraft, M.W. Dewhirst, Anticancer Action of Mn Porphyrins in Head and Neck Cancer BT - Redox-Active Therapeutics, in: I. Batinić-Haberle, J.S. Rebouças, I. Spasojević (Eds.), Springer International Publishing, Cham, 2016: pp. 469–484. https://doi.org/10.1007/978-3-319-30705-3_19.

[129] S. Chin, C.L. Eccles, A. McWilliam, R. Chuter, E. Walker, P. Whitehurst, J. Berresford, M. Van Herk, P.J. Hoskin, A. Choudhury, Magnetic resonance-guided radiation therapy: A review, J.

Med. Imaging Radiat. Oncol. 64 (2020) 163–177. https://doi.org/https://doi.org/10.1111/1754-9485.12968.

[130] J.A. Nelson, U. Schmiedl, E.G. Shankland, Metalloporphyrins as tumor-seeking MRI contrast media and as potential selective treatment sensitizers, Invest. Radiol. 25 (1990) S71–S73. https://doi.org/10.1097/00004424-199009001-00034.

[131] S. Nakajima, N. Shigemi, N. Murakami, T. Aburano, I. Sakata, I. Maruyama, M. Inoue, T. Takemura, Therapeutic and imaging capacity of tumor-localizing radiosensitive Mn-porphyrin on SCCVII tumor-bearing C3H/He mice, Anticancer. Drugs. 8 (1997) 386–390. https://doi.org/10.1097/00001813-199704000-00012.

[132] S. Shao, V. Rajendiran, J.F. Lovell, Metalloporphyrin nanoparticles: Coordinating diverse theranostic functions, Coord. Chem. Rev. 379 (2019) 99–120. https://doi.org/https://doi.org/10.1016/j.ccr.2017.09.002.

[133] M. Ethirajan, Y. Chen, P. Joshi, R.K. Pandey, The role of porphyrin chemistry in tumor imaging and photodynamic therapy, Chem. Soc. Rev. 40 (2011) 340–362. https://doi.org/10.1039/B915149B.

[134] S. Jenni, A. Sour, Molecular Theranostic Agents for Photodynamic Therapy (PDT) and Magnetic Resonance Imaging (MRI), Inorganics 7 (2019). https://doi.org/10.3390/inorganics7010010.

[135] S. Kunjachan, J. Ehling, G. Storm, F. Kiessling, T. Lammers, Noninvasive Imaging of Nanomedicines and Nanotheranostics: Principles, Progress, and Prospects, Chem. Rev. 115 (2015) 10907–10937. https://doi.org/10.1021/cr500314d.

[136] G. Chen, I. Roy, C. Yang, P.N. Prasad, Nanochemistry and Nanomedicine for Nanoparticle-based Diagnostics and Therapy, Chem. Rev. 116 (2016) 2826–2885. https://doi.org/10.1021/acs.chemrev.5b00148.

[137] M. Björnmalm, K.J. Thurecht, M. Michael, A.M. Scott, F. Caruso, Bridging Bio–Nano Science and Cancer Nanomedicine, ACS Nano. 11 (2017) 9594–9613. https://doi.org/10.1021/acsnano.7b04855.

[138] A.S.L. Derycke, P.A.M. de Witte, Liposomes for photodynamic therapy, Adv. Drug Deliv. Rev. 56 (2004) 17–30. https://doi.org/https://doi.org/10.1016/j.addr.2003.07.014.

[139] D. Feng, Z.-Y. Gu, J.-R. Li, H.-L. Jiang, Z. Wei, H.-C. Zhou, Zirconium-Metalloporphyrin PCN-222: Mesoporous Metal–Organic Frameworks with Ultrahigh Stability as Biomimetic Catalysts, Angew. Chemie Int. Ed. 51 (2012) 10307–10310. https://doi.org/https://doi.org/10.1002/anie.201204475.

[140] M. Yang, J. Deng, D. Guo, Q. Sun, Z. Wang, K. Wang, F. Wu, Mitochondria-targeting Pt/Mn porphyrins as efficient photosensitizers for magnetic resonance imaging and photodynamic therapy, Dyes Pigm. 166 (2019) 189–195. https://doi.org/10.1016/j.dyepig.2019.03.048.

[141] Y.Y. Liu, Y. Huang, B.P. Osei, Q. Zhang, Y.Y. Liu, M. Hua, Synthesis and in vitro evaluation of manganese (II)-porphyrin modified with chitosan oligosaccharides as potential MRI contrast agents, Chem. Res. Chin. Univ. 30 (2014) 549–555. https://doi.org/10.1007/s40242-014-4015-0.

[142] R. Canaparo, G. Varchi, M. Ballestri, F. Foglietta, G. Sotgiu, A. Guerrini, A. Francovich, P. Civera, R. Frairia, L. Serpe, Polymeric nanoparticles enhance the sonodynamic activity of meso-tetrakis (4-sulfonatophenyl) porphyrin in an in vitro neuroblastoma model, Int. J. Nanomed. 8 (2013) 4247–4263. https://doi.org/10.2147/IJN.S51070.

[143] G. Varchi, F. Foglietta, R. Canaparo, M. Ballestri, F. Arena, G. Sotgiu, A. Guerrini, C. Nanni, G. Cicoria, G. Cravotto, S. Fanti, L. Serpe, Engineered porphyrin loaded core-shell nanoparticles for selective sonodynamic anticancer treatment, Nanomedicine. 10 (2015) 3483–3494. https://doi.org/10.2217/nnm.15.150.

[144] P. Huang, X. Qian, Y. Chen, L. Yu, H. Lin, L. Wang, Y. Zhu, J. Shi, Metalloporphyrin-Encapsulated Biodegradable Nanosystems for Highly Efficient Magnetic Resonance Imaging-Guided Sonodynamic Cancer Therapy, J. Am. Chem. Soc. 139 (2017) 1275–1284. https://doi.org/10.1021/jacs.6b11846.

[145] B. Du, X. Yan, X. Ding, Q. Wang, Q. Du, T. Xu, G. Shen, H. Yao, J. Zhou, Oxygen Self-production Red Blood Cell Carrier System for MRI Mediated Cancer Therapy: Ferryl-Hb, Sonodynamic and Chemical Therapy, ACS Biomater. Sci. Eng. 4 (2018) 4132–4143. https://doi.org/10.1021/acsbiomaterials.8b00497.

[146] A.H. Soloway, W. Tjarks, B.A. Barnum, F.-G. Rong, R.F. Barth, I.M. Codogni, J.G. Wilson, The Chemistry of Neutron Capture Therapy, Chem. Rev. 98 (1998) 1515–1562. https://doi.org/10.1021/cr941195u.

[147] R.F. Barth, J.A. Coderre, M.G.H. Vicente, T.E. Blue, Boron Neutron Capture Therapy of Cancer: Current Status and Future Prospects, Clin. Cancer Res. 11 (2005) 3987 LP – 4002. https://doi.org/10.1158/1078-0432.CCR-05-0035.